Synthesis of (1-x) [$Bi_{0.9}Eu_{0.1}FeO_3$] + x [$Ni_{0.6}Zn_{0.4}Fe_2O_3$] Nanostructured Multiferroic Composites and Study of its Structural, Magnetic and Electrical Properties

M. Sc. Thesis

By

AL-Masud

DEPARTMENT OF PHYSICS
KHULNA UNIVERSITY OF ENGINEERING & TECHNOLOGY
KHULNA - 9203, BANGLADESH

MAY – 2018

Synthesis of (1-x) $[Bi_{0.9}Eu_{0.1}FeO_3]$ + x $[Ni_{0.6}Zn_{0.4}Fe_2O_3]$ Nanostructured Multiferroic Composites and Study of its Structural, Magnetic and Electrical Properties

By

AL-Masud
ROLL No. 1655552
SESSION: JULY - 2016

A THESIS SUBMITED TO THE DEPARTMENT OF PHYSICS,
KHULNA UNIVERSITY OF ENGINEERING & TECHNOLOGY,
KHULNA - 9203 IN PARTIAL FULFILMENT OF THE
REQUIRMENT FOR THE DEGREE OF MASTER OF SCIENCE

DEPARTMENT OF PHYSICS
KHULNA UNIVERSITY OF ENGINEERING & TECHNOLOGY
KHULNA - 9203, BANGLADESH

MAY - 2018

TO

MY PARENTS

DECLARATION

This is to certify that the thesis work entitled "Development and Performance Evaluation of Storage Allocation Models in Warehouse" has been carried out by Md. Saiful Islam in the department of Industrial engineering and management, Khulna University of engineering & technology, Khulna, Bangladesh. The above research work or any part of the work has not been submitted anywhere for the award of any degree or diploma.

Signature of Supervisor

Signature of Candidate

APPROVAL

This is to certify that the thesis work submitted by Md. Saiful Islam entitled "Development and Performance Evaluation of Storage Allocation Models in Warehouse" has been Approved by the Board of Examiners for the partial fulfillment of the requirements for the degree of Master of Science in Engineering in the Department of Industrial Engineering and Management, Khulna University of Engineering & Technology, Khulna-9203, Bangladesh in November 2018.

BOARD OF EXAMINERS

1. _____ 8/11/18

Md. Kutub Uddin — Chairman (Supervisor)
Professor
Department of Mechanical Engineering
Khulna University of Engineering & Technology

2. _____ 08.11.18

Dr. Azizur Rahman — Member
Associate Professor & Head
Department of Industrial Engineering and Management
Khulna University of Engineering & Technology

3. _____ 8/11/18

Dr. Md. Rafiquzzaman — Member
Assistant Professor
Department of Industrial Engineering and Management
Khulna University of Engineering & Technology

4. _____ 8/11/18

Dr. Engr. Mohammad Iqbal — Member (External)
Professor
Department of Industrial & Production Engineering
Shahjalal University of Science and Technology

Acknowledgements

I would like to express my deepest sense of gratitude and high gratefulness with due respect to my Supervisor Professor Dr. Shibendra Shekher Sikder, Department of Physics, Khulna University of Engineering & Technology (KUET), Khulna for considering me as a thesis student. His guidance, enthusiastic concern, positive and regular inspiration and constructive supervision throughout the time made the work easy and successful.

I am very much indebted to my Co-Supervisor Dr. Abdul Gafur, Senior Engineer, PP & PDC, Bangladesh Council of Scientific and Industrial Research (BCSIR), Dhanmondi, Dhaka-1205, Bangladesh for introducing the present research topic and inspiring guidance and valuable suggestion of this research work, who has consistent support and necessary motivation to progress my experimental works.

I gratefully acknowledge Professor Dr. Md. Mahbub Alam, Head, Department of Physics, KUET, for his support, words of encouragement, direction and help to shape up my thesis.

I am grateful to Dr. S. Manjura Hoque, Head & Chief Scientific Officer, Materials Science Division (MSD), Atomic Energy Centre, Dhaka (AECD) for providing kind opportunity to use the laboratory for experimental work. My thanks are also for Dr. Mohammed Nazrul Islam Khan, Principal Scientific Officer (PSO), MSD, AECD, for his and providing necessary ideas about this research. His valuable direction, suggestions and continuous assessment on work made me conscious and sincere to obtain better results in all experiments. Without his help and support it was quite difficult to do the research.

I would like to express my special gratitude and thanks to A. K. M Atique Ullah, Senior Scientific Officer, AECD, for using his lab and imparting his knowledge and expertise in this research work. I would also indebted to Mr. Abu Raihan Tarek, Chemistry Division, AECD, for supporting me to use his lab and guidance on synthesizing materials.

I want to give my warm and deep gratitude to Dr. M. A. Matin, Head, Department of Glass & Ceramic Engineering (GCE), Bangladesh University of Engineering & Technology (BUET), for his honest and cooperative response to me and providing permission to use the FESEM facilities of his department.

I am also grateful to Professor Dr. Md. Abdullah Elias Akhter, Department of Physics, KUET, for his support and words of encouragement. I gratefully acknowledge Professor Dr. Joly Sultana, Department of Physics, KUET, for his co-operation and inspiration during this work. My thanks are also for Md. Kamrul Hasan Reza (Associate Professor), Mr. Sujit Kumar Shil (Assistant Professor), Sumon Kumar Halder (Assistant Professor), Sifullah (Lecturer), for their moral support.

I would like to thank Mr. Alamgir Hossain (Assistant Professor), for his support, suggestions and provisions that benefited me much in the completion of this thesis work. I place on record my gratitude to Sumon Debnath (Lecturer), Department of Physics, KUET, for his sincere and valuable guidance and encouragement extended to me. I also thank Probal Roy (Lecturer), Department of Physics, KUET, for his advices and valuable comments on my thesis.

My special thanks to all the staff members of Materials Science Division and Chemistry Division, AECD, particularly Mrs. Alhamra Parveen, Mrs. Anjuman Ara Begum, Mr. Kamrul Islam, Mr. Anowar Hossain, Mr. Nurul Islam, Mrs. Nazmunnahar Begum, Mrs. Zarna Begum and Mr. Kaiyoum, Mr. Jahid, Mr. Ayub and Mr. Zahid for their sincere help during the preparation of the sample and experimental measurements.

I am highly indebted and thoroughly grateful to Md. Rabiul Hassan for his great effort from the very beginning of this research work. It is really hard for me to cope-up with this without his help and motivation.

Special thanks to Md. Forhad Hossain and Mohammad Moniruzzaman for providing their kind help throughout this work. Without their help, it was really hard for me to continue my work in Atomic Energy Centre, Dhaka.

I would like to give thanks from deep of my heart to my parents and all others family members for their comprehensive mental support and love. I have not much word to express my gratefulness to them.

I also wish to thank to the authority of Khulna University of Engineering & Technology for providing me the necessary permission for conducting the thesis work.

Al - Masud

Abstract

Multiferroic Composites with different mass ratio of Europium doped Bismuth Ferrite (BEFO) and Nickel Zinc Ferrite (NZF) with general formula (1-x) [$Bi_{0.9}Eu_{0.1}FeO_3$] + x [$Ni_{0.6}Zn_{0.4}Fe_2O_4$] for various x values (x=0, 0.1, 0.3, 0.5, 0.7 and 1) have been prepared by the conventional solid-state reaction method aided with different dispersion techniques like magnetic stirring, power ultrasonification and centrifugation. Crystallinity and structure of the samples were investigated by powder X-ray diffraction and distorted rhombohedral perovskite BEFO and cubic NZF has been observed for x = 0.0 and x = 1.0. Mixed perovskite-spinel structure has been observed for the composites which prove that in the composite BEFO and NZF phases coexist together with no chemical reaction. The formation of nano is observed through FESEM micrographs and the compositional purity of the prepared samples has been confirmed by Energy dispersive x-ray Spectra (EDX). To understand the temperature dependent grain growth of the samples, all the samples were heated at 300^0 C, 450^0 C, 600^0 C, 750^0 C and 850^0 C and the average grain size has been observed in between (65 ~ 75) nm, (65 ~ 70) nm, (55 ~ 70) nm, (350 ~ 400) nm and (750 ~ 800) nm respectively. The ferromagnetic hysteresis behavior of the samples have been obtained through vibrating sample magnetometer (VSM) and the magnetic properties such as saturation magnetization (M_s), remanent magnetization (M_r), coercive field (H_c), molecular magnetic moment (μ_B) and magnetic anisotropy constant are calculated from it. It has been observed that M_s has increased with increasing NZF content. The complex permeability (μ) of the prepared samples have been measured and a fairly constant initial permeability (μ') has been observed over a wide range of frequency (~10^8 Hz) region. Dielectric properties and AC conductivity of the samples have been studied in a wide range of frequencies from 1Hz to 100MHz at room temperature by impedance analyzer and found that x = 0.1 shows the maximum dielectric constant. Dielectric dispersion has been observed at lower frequency (< 10^5 Hz) and is attributed to the interfacial polarization. The complex impedance spectroscopy is used to correlate between the electrical properties of the studied samples with their microstructure. The optimum composition is observed for x = 0.1 which possess the highest frequency dependent dielectric constant and permeability with lower dielectric and magnetic loss.

Contents

CHAPTER-III

EXPERIMENTAL PROCEDURE

CHAPTER-IV
RESULTS AND DISCUSSION

CHAPTER-V
CONCLUSIONS

List of Figures

List of Tables

List of Symbols

XRD	=	X-Ray Diffraction
VSM	=	Vibrating Sample Magnetometer
FESEM	=	Field Emission Scanning Electron Microscopy
BEFO	=	$Bi_{0.9}Eu_{0.1}FeO_3$
NZF	=	$Ni_{0.6}Zn_{0.4}Fe_2O_4$
ρ_b	=	Bulk density
ρ_x	=	X-ray density
M_S	=	Saturation magnetization
K_1	=	Anisotropy constant
H_c	=	Coercive force
μ_B	=	Magnetic moment
μ	=	Permeability
μ'	=	Real part of the complex permeability
μ''	=	imaginary part of the complex permeability
ε	=	Permeability
ε'	=	Real part of the dielectric constant
ε''	=	imaginary part of the complex permeability
D	=	Grain size
B	=	Magnetic induction
H	=	Magnetic field
a	=	Lattice parameter
tan δ	=	loss factor or loss tangent.
λ	=	Wave length of the X-ray
[hkl]	=	Index of the peak

CHAPTER I

INTRODUCTION

INTRODUCTION

1.1 Introduction

Humans are great taking lumps of stuff and making them useful. This approach of making and engineering products begins from the very early age of the human civilization. Influence of materials at that time was so high that the first three ages of human civilization were named after materials i.e., Stone age, Bronze age, Iron age. At the Stone Age, people develop material just to survive and hunting purposes [1.1]. Material development at that ages were confined only on the materials our ancestors could mine or grow or otherwise collect, what they could see with their eyes and what they could touch with their hands.

Design of new material is not an easy task. For that reason, every stage of civilization costs many times to jump another stage. The field of research we describing typically involves terms such as 'multiferroic' and 'magneto electric'. By original definition, a single-phase multiferroic [1.2] material is one that possesses two or all three of the so called 'ferroic' properties: ferroelectricity, ferromagnetism and ferroelasticity. A confluence of three factors explains the current high level of interest in magneto electrics (ME) and multiferroic material. First, Nicola Hill [1.3] discussed the condition required for ferroelectricity and ferromagnetism to be compatible in oxides, which in effect issued a grand material development challenge which was taken up because empirically there are indeed few multiferroic materials. Second, the experimental machinery for the synthesis and study of various contenders was already in place. Third, the relentless drive towards ever better technology is aided by the study of novel materials.

An increase of interest in multiferroics was started around 2003, with the discovery of magnetically induced ferroelectricity. These include Local density approximation (LDA), Generalized gradient approximations (GGA), Local spin-density approximation (LSDA), + U Coulomb interaction, Berry-phase approach and many more. New approach experimental methods that allow the observation of magnetic and electric domains. Recent successes in the synthesis of complex oxides structures can be realized with atomic level precision of multiferroic materials which have promising future application especially in digital technologies. This is important

to know that how fast a material can convert '0' to '1' by altering the magnetization field with significant saturation magnetization (Ms). To enable spontaneous conversion from '0' to '1' and '1' to '0' it is required to frequent change in magnetization with changing electric field. Multiferroic material is a term in solving such problems where we get both ferroelectric and ferromagnetic properties. The demand of materials with multifunctional properties is increasing with development toward device miniaturization. Multiferroics are such functionable materials and have become a hot topic of research in recent years.

Multiferroic materials have returned to the forefront of materials research. Driven by the desire to achieve new functionalities such as electrical control of ferromagnetism at room temperature and have undertaken a concerted effort to identify and understand the complexities of multiferroic materials. They have wide range of technological application in transformer cores, inductors, high quality filters, radio frequency circuits, rod antenna, read/write heads for high-speed digital tape and operating devices [1.4 - 1.6].

Despite these, Multiferroic has become more interesting due to their ability of coupling the electric and the magnetic polarization, which offers an extra degree of freedom in the design and multifunctional applications [1.7 - 1.8]. For example, recently it has been demonstrated that it is possible to switch and control local ferromagnetism with an electric field exploiting the multiferroic properties of bismuth ferrite $BiFeO_3$ (BFO), which in turn are expected to greatly reduce the writing energy of magnetic random access memory (MRAM) elements and paving the way for the so-called ME random access memory (MeRAM) elements [1.9]. BFO is one of the most importantly studied and promising multiferroic materials, which has a relative simple structure and at the same time uncommon properties: BFO possess two coupled order parameters (ferroelectricity and antiferromagnetism) at room temperature [1.10 - 1.11]. More over BFO sets a standard in the global search for new multiferroic materials where ME coupling is weak.

In the recent years, the multiferroic composite materials have attracted a significant interest all over the world from the technological as well as academics point of view [1.12]. These materials are useful as magnetic field sensors (ac and dc field measurement), actuators, transducers, phase shifter, filters and memory devices. In spintronics devices multiferroic materials have wide range of applications in modern electronics for their successive phenomena both in electric and magnetic

purposes. Multiferroics exhibits several kinds of long range magnetic ordering, spontaneous electric polarization and ferroelectricity [1.13]. BFO is one of the popular materials in the sense of having significant multiferroic properties. Both its antiferromagnetic and ferroelectric transition temperatures (643 K and 1100 K, respectively) are well above room temperature [1.14]. BFO shows excellent ferroelectric and piezoelectric properties at room temperature. The piezoelectric coefficient is approximately 50 pm/V. The large piezoelectric coefficient shows that BFO is also well-suited for the ME coupling. The magnetic behavior of the composites at room temperature display magnetic hysteresis loop indicates that the composite are ferromagnetic [1.15]. The dielectric and magnetic properties of ferroelectric–antiferroelectric $BaTiO_3$-$LaMnO_3$ composite with sintering temperature, i.e. 1150^oC, the Ba ion in $BaTiO_3$ seems to diffuse into $LaMnO_3$; resulting in $BaTiO_3$-(La, Ba)MnO_3 ferroelectric-ferromagnetic composite [1.16].

In this study, multiferroics composite has been synthesized to examine physical, magnetic, electrical and structural properties. The designed composite material will have the form (1-x)[$Bi_{0.9}Eu_{0.1}FeO_3$] + x[$Ni_{0.6}Zn_{0.4}Fe_2O_4$]. Europium is magnetically active and it reduces the leakage current density of $BiFeO_3$ effectively so Eu will be doped in the A-site of BFO to improve its weak ferromagnetic and dielectric behaviors. NZF will be designed with 60% Ni and 40% Zn which shows strong ferromagnetic behavior with low eddy current losses. Therefore, it is quite interesting to look at possible changes in the various physical properties of a class of BEFO–NZF composites.

1.2 Motivation

Use of multiferroics is not popular in Bangladesh, and only studying in a small scale at the research level. But with the economic and industrial development, a potential requirement of multiferroics has developed here. And this requirement has become more intense when this country started her journey to the digital world. To make her journey to the digital world, she requires all the corresponding accessories. Moreover, a revolution has done here in computer sectors and mobile devices within just a few years. But a matter of sadness is that still now, the research on improving electronic devices like memory devices, microprocessor, inductors, transducers etc. are not appreciated from the point of research interest. Without contributing on

hardware development, it will be quiet tough to achieve the goal of digital Bangladesh.

Multiferroic composites may consider as a potential candidate to solve such problems. Recently it has been demonstrated that it is possible to switch and control local ferromagnetism with an electric field exploiting the multiferroic properties of BFO, which in turn are expected to greatly reduce the writing energy of magnetic random access memory (MRAM) elements and paving the way for the so-called ME random access memory (MeRAM) elements [1.9]. Bismuth ferrite has ferroelectric photovoltaic effect. Nanoscale BFO with expanded surface area can absorb much more solar radiation to produce more photocurrent. So BFO doped solar cell can be a potential source of cleaner safer and affordable modes of energy [1.17]. So to obtain nano-particle has been proposed in this research. NZF have been found to be one of the most versatile of the ferrite systems with strong ferro-magnetic behaviour. A suitable combination of ferroelectric BEFO with strongly magnetic NZF will be very significant to get better ME effect. This research (1-x) $[Bi_{0.9}Eu_{0.1}FeO_3]$ + $x[Ni_{0.6}Zn_{0.4}Fe_2O_4]$ will suggest this composition.

To synthesis nano, I will use conventional solid state reaction method with different dispersion techniques. Though it is an energy consuming monotonous process, it is the most friendly and widely used method. The advantage of this method is that, it is a low cost process with higher productivity, and the filing properties of this method are also better. In liquid state reaction (like sol-gel method, chemical co-precipitation method, hydrothermal method, sol-gel auto-combustion method) methods, it requires a solvent, which is very costly. Also there is a question of PH control, where one can easily be fused. Moreover, once the reaction completed, one need to remove the residual solvent from the resulting product, which is again a time consuming event. In solid state reaction method, as there is no solvent, there is no waste to remove and therefore more friendly.

The one drawbacks of solid state reaction method is that, the prepared substance is not in that homogeneous as in the liquid state reaction. To lessen this drawback, different dispersion techniques like elevated stirring in the magnetic stirrer and power sonication in the ultrasonic bath will be applied. It will help to mix and disperse the substances to increase their homogeneity and quality. This fabrication of BEFO-NZF composites has done to improve not only their ferroic order but also the other properties like dielectric, conductivity, impedance etc. Obtain nano-particle is a

goal to this research and the effect of increasing annealing temperature with grain growth will also be studied.

1.3 The Aims and Objectives of the Present Work

The main objective of the present work is to synthesize nanostructured multiferroic composite with composition (1- x) $[Bi_{0.9}Eu_{0.1}FeO_3]$ + x$[Ni_{0.6}Zn_{0.4}Fe_2O_4]$ where [x = 0.0, 0.1, 0.3, 0.5, 0.7 and 1.0]. The objectives of the research works are as follows:

- To synthesize $[Bi_{0.9}Eu_{0.1}FeO_3]$ and $[Ni_{0.6}Zn_{0.4}Fe_2O_4]$ nanostructured phases by conventional solid state reaction with different dispersion techniques and multiferroic composite with composition (1-x)$[Bi_{0.9}Eu_{0.1}FeO_3]$ + x$[Ni_{0.6}Zn_{0.4}Fe_2O_4]$ where [x = 0.0, 0.1, 0.3, 0.5, 0.7 and 1.0].
- To mix the samples by agate and mortar with acetone as mixing media.
- In dispersion method the sample will be stirred in magnetic stirrer with pure acetone, dispersed by ultrasonic bath and washed by distilled water in centrifuge.
- Sample will be dried in microwave oven at 100^0C and sintered at 600^0C for 4 hours in a furnace to remove other light ingredients.
- To study the crystalline phase of the prepared samples by XRD.
- To study the surface morphology and grain growth by FESEM.
- To obtain magnetic hysteresis and saturation magnetization by VSM.
- To study the dielectric properties and initial permeability as a function of frequency by impedance analyzer.

1.4 Experimental Reason for this Research Work

The multiferroic composites will be prepared with highly pure materials by using conventional solid state reaction method with different dispersion techniques. High purity powders of NiO (99.9%); ZnO (99.9%); Fe_2O_3 (99.99%); Bi_2O_3 (99.9%) and Eu_2O_3 (99.9%), has been mixed thoroughly in an appropriate amount in both dry and acetone media. The mixed powder will be stirred in magnetic stirrer and dispersed in ultrasonic bath and washed by distilled water in centrifuge. The powder sample will be dried and pre-sintered at 600^0C for 4 hours. After Pre-sintering toroid and disk shaped samples will be prepared and sintered at 850^0C for 3 hours. The experimental methods will be used in this research work as follows:

- The samples will be mixed by agate and mortar as well as using conventional ceramic technique.
- Nanostructure formation will be confirmed by XRD and FESEM.
- Frequency dependent permeability will be obtained by Impedance analyzer.
- AC resistivity, dielectric constant will be obtained by Impedance analyzer.
- Magnetization, M-H loop, coercivity, retentivity etc will be measured from VSM data.

It is expected that the explored composites have large electric polarization and magnetization with small loss at room temperature and will be useful applications. Our work may suggest a new approach for the design of multiferroics, composed of two compounds with same crystal structure.

1.5 Background of Material Selection: Literature Review

Materials with pronounced magnetic and electric properties permeate everywhere in modern technology and modern life. Multiferroic materials are attractive have the properties of both magnetic and ferroelectric compounds, but also the magneto electric coupling leads to additional function. The current trend towards device miniaturization has led the interest in combining electronic and magnetic properties into multifunctional material. New type of devices for electric field controlled magnetic memory data storage on the basis of magneto electric effect. In this research, the proposed sample has the formula of (1- x) $[Bi_{0.9}Eu_{0.1}FeO_3]$ + x$[Ni_{0.6}Zn_{0.4}Fe_2O_4]$ where x = 0.0; 0.1; 0.3; 0.5; 0.7 and 1.0. The reason of material selection has been attributed to the study of common problems with $Bi_{0.9}Eu_{0.1}FeO_3$ (BEFO) and $Ni_{0.6}Zn_{0.4}Fe_2O_4$ (NZF). The literatures are given below:

1.5.1 Europium Doped Bismuth Ferrite (BEFO)

BFO is one of the most studied room temperature multiferroic material, which fascinates the scientist community over the past few decades. Despite its strong ferroelectric properties, it shows G-type antiferromagnetic ordering with spiral spin structure with periodicity 620A^o which leads to the cancellation of any macroscopic magnetization, thus inhibits the linear ME effects [1.18]. Thus even though BFO has T_C and T_N well above the room temperature, its potential applications are yet to be fully realized. Hence any efforts of including the ferromagnetism in BFO while retaining the FE will be rewarding technologically and also is a basic research

problem. Over the past few decades there had been several works on the improvement of multiferroic property of BFO. The improvement in the ME coupling is achieved by the reduction of particle size below the spiral period order (62 nm) which leads to the breaking of the incommensurate spiral-spin structure and antiferromagnetic ordering. The multiferroic property is further improved by A-site [1.18- 1.27], B-site [1.28 - 1.29] and both A - B site [1.29 - 1.30] doping strategy with alkaline earth metal [1.30], rare earth metal [1.19, 1.21, 1.25, 1.28] and transition metal ions [1.30].

For instance, Dai *et al.* [1.31] investigated that, the dielectric constant, dielectric loss and their frequency response were changed dramatically by substitution of Eu for Bi. The dielectric loss was effectively decreased with increasing Eu content. In addition the leakage current measurements showed that the substitution of Eu effectively reduced the leakage current density of BFO ceramics.

Freitas *et al.* [1.32] reported the microstructural and magnetic property of 5 mole% Eu doped BFO and concluded that a low degree substitution of Eu is enough to break the colloidal spin arrangement of BFO to enhance the magnetic coercivity preserving its structural and microstructural characteristics. Liu et al. [1.33] studied the enhancement of magnetization in Eu doped BFO and said that the magnetically active characteristic of Eu^{3+} ions and the appearance of europium orthoferrite are responsible for the observed high magnetization values in BEFO.

Zhang *et al.* [1.34] reported the composition driven phase transition in Eu doped BFO with enhanced multiferroic property and suggested that ME coupling exists in these compounds. Recently Banerjee *et al.* had identified a large enhancement in multiferroic, coercive field as well as an increase in exchange bias in nanocrystalline Eu doped BFO. They concluded that the enhanced coercivity and exchange bias will increase its potential for future application in random access memory devices e.g., MeRAM, FeRAM etc.

1.5.2 Nickel Zinc Ferrite (NZF)

As an important member of ferrite family, NZF ferrites have attracted significant research interest based on its fascinating magnetic and electromagnetic properties. They exhibit high electrical resistivity, high permeability, compositional stability and low eddy current losses [1.35 - 1.38] especially ideal for high frequency applications. As soft magnetic material NZFs are promising candidates for manufacturing of multilayer chip inductors [1.39]. Brito *et al.* [1.40] reported that

NZF nanoparticles show higher resistivity, relatively higher permeability and lower eddy current loss compared to its bulk form. Matsushita *et al.* [1.41] investigated that NZF have a good utility as a conducted noise suppressor material in various electromagnetic interfaces. Researchers have also reported the structural, electrical and/or dielectric properties of doped NZF. Recently, many researchers reported the structural, magnetic and electrical properties of NZF and/or substituted NZF in bulk [1.42-1.49] and nano forms [1.50-1.53].

1.5.3 BEFO-NZF Multiferroic Composites

The ME effect arises in single-phase multiferroics is solely due to the coupling of their intrinsic magnetic and electric orders and is either relatively weak or occurs at temperatures too low for practical applications. But multiferroic composites incorporate independent ferroelectric and ferri/ferromagnetic phases yield giant ME coupling effect [1.54]. Dhanalakshmi *et al.* [1.55] in her work, successfully prepared perovskite-spinel di-phase BFO-NZF and Mn doped BMFO-NZF composites and reported that BMFO-NZF composite was effectively in reducing the conductivity, dielectric losses and also improving impedance properties. Adhlakha *et al.* [1.56] found the ME coupling between BFO-NZF composites and observed enhanced multiferroic and optical properties. He attributed ferromagnetic behaviors to the collapse of the spin cyclical structure of BFO. Mazumder *et al.* [1.57] prepared BFO-NCZF composite by standard solid state reaction route and reveals the coexistence of both the ferroelectric and ferrite phase in the composite and found excellent frequency stability in the high frequency region. In the past years, various magneto electric composites have been developed such as $CoFe_2O_4$-$BaTiO_3$ [1.58], $NiFe_2O_4$-$BaTiO_3$ [1.59], $Ni_{0.8}Zn_{0.2}Fe_2O_4$-$Ba_{0.6}Sr_{0.4}TiO_3$ [1.60], (x)$Co_{0.5}Zn_{0.5}Fe_2O_4$ -(1-x)PLZT [1.61], and $BiFe_{0.5}Cr_{0.5}FeO_3$–$NiFe_2O_4$ [1.62].

1.6 Outline of the Thesis

The thesis has been configured into five chapters which are as follows:

Chapter I: Introduction

In this chapter, a brief introduction to multiferroic composite with composition (1- x) $[Bi_{0.9}Eu_{0.1}FeO_3]$ + x$[Ni_{0.6}Zn_{0.4}Fe_2O_4]$ nanostructure ferrites and organization of thesis. This chapter incorporates background information to assist in understanding

the aims and objectives of this investigation and also reviews recent by other investigators with which these results can compared.

Chapter II: Theoretical Background

In this chapter, a briefly describe theories necessary to understand overview of multiferroic, single phase multiferroic, multiferroic composite and nanostructure multiferroic, ferromagnetism and multiferroicity etc have the present work in details.

Chapter III: Experimental Procedure

In this chapter, the experiment procedures are briefly explained along with description of the sample preparation, raw materials, methodology of nanostructure multiferroic composites preparation. The fundamental and working principles of measurement set up are discussed.

Chapter IV: Results and Discussion

In this chapter, results and discussion are thoroughly explained. The XRD analysis, representation of XRD data , study of microstructure with various isothermal stage, magnetization of ferromagnetic effect on multiferroic with experimental samples and measurement of ferroelectric properties of multiferroic composite with composition (1-x).BEFO + x.NZF nanostructure ferrites are presented.

Chapter V: Conclusions

In this chapter, the results obtained in this study are summarized. Suggestions for future works on these studies are included.

References are added at the end of each chapter.

CHAPTER II

THEROETICAL BACKGROUND

THEORETICAL BACKGROUND

2.1 Overview of Multiferroic

A ferroic material is basically a material which exhibits one of the three (currently expanded to four) ferroic ordering: ferroelectricity, ferromagnetism, ferroelasticity, or ferrotoroidicity. The common feature of the four types of ferroic ordering is the spontaneous electrical polarization, magnetization, strain or toroidal moment, in a phase transition from a high-temperature prototype phase to the low-temperature ferroic phase. The material also shows well defined hysteresis loop, when it switched electrically, magnetically, mechanically or with the change of toroidal source vector respectively [2.1].

Multiferroics are one class of unique functional materials that exhibit two or more of the above ordering mechanism and have attracted considerable interest due to the coexistence of at least two switchable states (e.g., polarization, magnetization and strain), which promises a wide range of applications in multifunctional devices. For example, one can have multi-state memory element or sensors which can be operated in multi-mode or spintronic devices, ferroelectric information recording, ceramic ultrasound transducers, frequency tunable resonators, phase shifters etc [2.2].

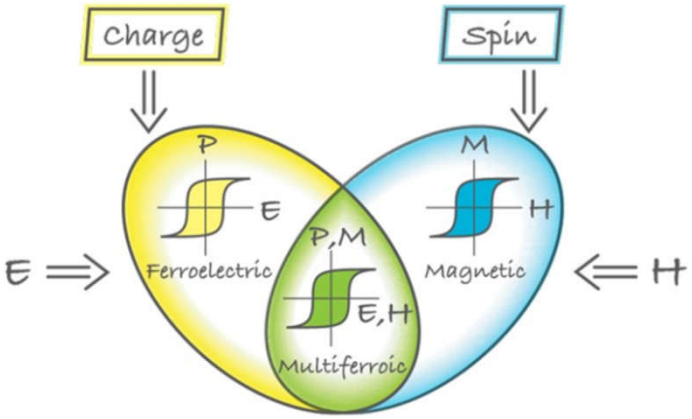

Figure 2.1: Ferroelectric and magnetic coupling in a multiferroic

Multiferroics usually combine the properties of ferroelectrics and ferromagnets. In the ideal case, the magnetization of a ferromagnetic in a magnetic field displays the usual hysteresis (blue), and ferroelectrics have a similar response to an electric field (yellow). If we manage to create multiferroics that are simultaneously

ferromagnetic and ferroelectric (green), then there is a magnetic response to an electric field and vice versa [2.3]. In multiferroic materials, the coupling interaction between the different order parameters could induce new physical effects: the magnetoelectric (ME) effect. The ME response is the appearance of an electric polarization **P** by an applied magnetic field **H** and the appearance of magnetization **M** by an electric field **E**.

$$\Delta P = \alpha_H \Delta H \qquad \text{and} \qquad \mu_0 \Delta M = \alpha_E \Delta \tag{2.1}$$

Where, μ_0 is the vacuum permeability, α_H and α_E are the ME coupling coefficient representing the coupling efficiency between the electric and magnetic fields [2.4].

However, there are very few materials in nature where ferroelectricity and magnetism can coexist, because these phenomena tend to exclude one another. For instance, all conventional FE perovskites contain transition metal ions with empty d-orbital (d^0), but on the other hand, magnetism is related to ordering of spins of electrons in incomplete ionic shells, which require partially filled d-orbital's (d^n). Therefore, as soon as we have at least one or more d-electrons, the material may be magnetic but never ferroelectric [2.5]. There are also some other contradictory behaviors between these two ferroic orders. Electrically while a ferroelectric material must be an insulator, most of the ferromagnetic materials are metallic or narrow band-gap semiconductors, which strongly discourage multiferroicity. Nevertheless, many research groups became involved studying the rare situation of coexisting order parameters and their coupling.

2.2 Types of Multiferroic

From the viewpoint of material constituents, multiferroic materials can essentially be divided into two types:

(1) Single-phase Multiferroic Material.

(2) Composite Multiferroic material.

2.2.1 Single-phase Multiferroic Material

Single-phase multiferroic materials are defined as homogenous compounds in which electric and magnetic order coexist at any point or given location within the material. However, the occurrence of magnetic and electric order in the same phase is very rare in nature and also very difficult to prepare artificially. The reasons behind the scarcity of single-phase multiferroics have been analyzed by Hill in her paper [2.6] where she argued that transition metal d-electrons play the role behind this.

However, another research group thinks that multiferroicity is restricted by strict symmetry conditions. They showed that crystals with ferroelectric properties possess time reversal symmetry but do not show space inversion symmetry. Whereas, ferromagnetic materials possess space inversion symmetry but not time inversion symmetry, which strongly discourage multiferroicity. The total number of possible crystal structures is 122, as given by the Shubnikov point groups [2.7]. Out of all 122 possible point groups, there are 31 crystallographic point groups permitting electric phase and 31-point groups allowing magnetic phase. Shuvalov and Belov showed that 13 crystallographic point groups are found in both sets that allow electric and magnetic order to coexist in the same phase (i.e., multiferroic crystals) [2.8 - 2.9]. Single-phase multiferroics are further classified into two types: Type-I and Type-II multiferroics by Khomskii in 2009 [2.10].

Type-I: multiferroics are materials in which magnetic and electric phases coexist within the same compound, but have different microscopic origins which occur at different temperature and the effects are fairly independent of each other. Usually the structural distortion gives rise to the ferroelectricity which occurs at high temperature, and the magnetic ordering occurs at lower temperature. The prototypical example is $BiFeO_3$ (T_C = 1100 K, T_N = 643 K).

Type-II: multiferroics are materials in which ferroelectric order is induced by magnetism, which in turn suggests a very strong magneto-electric coupling. The ordering temperatures for the two phenomena are identical. In this case, the magnetic ordering breaks the inversion symmetry and directly causes the ferroelectricity. The prototypical example is $TbMnO_3$.

2.2.2 Multiferroic Composites Material

Although a great number of single-phase multiferroic compounds have been widely investigated, not a single material has been discovered to display large and technologically useful ME coupling at room temperature. Multiferroic composite materials were developed to solve this single phase multiferroics dilemma. Multiferroic composites are defined as compounds where electric, magnetic, and piezo orders coexist simultaneously and the order phases are physically separated from each other. Since the ferroic phases are fully separated within the composite, the requirement for ‘full dielectric’ as in the single-phase multiferroic is no longer

applicable here. The electric order phase is obviously a dielectric insulator, but the magnetic phase can be dielectric insulator or metallic conductor.

The limitations of single-phase multiferroics related to simultaneous spatial and time reversal symmetry breaking are completely eliminated in the case of composite multiferroics, as the symmetry condition is automatically fulfilled for any combination of materials in any possible geometry [2.11].

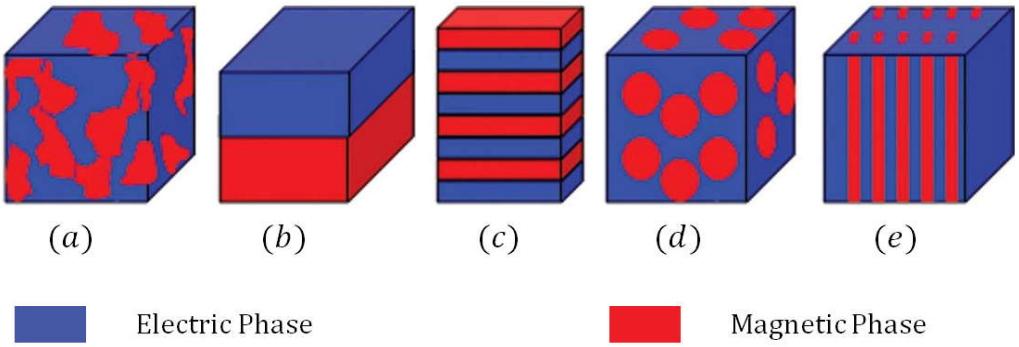

Figure 2.2: Diagrams of possible multiferroic composite structures. (a) Homogeneous mixture of electric and magnetic phases; (b) laminated bi-layer structure; (c) laminated multi-layer structure; (d) composite made of particles mixed in a matrix; and (e) fiber multiferroic composite. (adopted from 2.11)

Nevertheless, it is known that the ME effect in single phase magnetoelectrics can be solely due to the coupling of magnetic and electric orders only, but in multi-phase composite materials the effect originates from interface coupling effects and strain also [2.12]. It has been found that a much stronger ME coupling effect is expected to be realized in a composite of piezoelectric phase and magnetostrictive phase by using product properties [2.13]. The magnetostriction induces a mechanical deformation with the effect of an applied magnetic field, which is further mediated by mechanical stress and as a consequence, an electric field is induced due to the piezoelectric effect [2.14 - 2.16]. Composite materials may show sum properties or product properties [2.17 - 2.19]. The weighted sum of the contributions from individual phases, proportional to volume fraction of these phases gives rise to sum properties. For example, the physical quantities like density, magnetization, and dielectric properties come in category of sum properties.

The product property is more interesting which is absent in individual phases but is present in their composite. In composite materials, the ME effect comes as the 'product property' of the two phases in the composite and was first proposed by Suchtelen [2.19]. This effect in composites is due to the strain induced in the ferrite

phase by an applied magnetic field, which in turn induces a stress in the ferroelectric phase, thereby resulting of polarization in the ferroelectric phase due to the piezoelectric effect [2.20]. The composite ME effect can be described as follows

$$\text{Direct ME effect} = \frac{\text{magnetic}}{\text{mechanical}} \times \frac{\text{mechanical}}{\text{electric}}$$

$$\text{Converse ME effect} = \frac{\text{electric}}{\text{mechanical}} \times \frac{\text{mechanical}}{\text{magnetic}}$$

Many bulk ME composites have been found to exhibit such a strain-mediated ME effect above room temperature.

2.3 Spinel Ferrite and Its Structure

The spinels are any of a class of minerals of general formulation AB_2O_4 which crystallize in the cubic (isometric) crystal system. Normal spinel structures are generally cubic close-packed oxides with two tetrahedral and one octahedral site per formula unit. The tetrahedral spaces are tinier than the octahedral spaces. B^{3+} ions reside half the octahedral holes, while A^{2+} ions fill one-eighth of the tetrahedral holes. Bragg and Nishikawa first established its crystal structure [2.21].

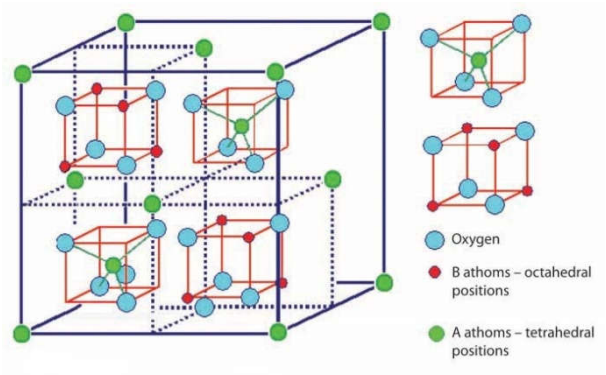

Figure 2.3: Schematic figure of spinel structure

On the other hand, if the A^{2+} ions occupy the octahedral voids, and half of B^{3+} ions occupy the tetrahedral voids, the structure is known as inverse spinel structure. In many spinel, an inter-mediate degree of inversion is possessed by the cation distribution where both sites have a fraction of A^{2+} and B^{3+} cations. Such spinels are referred as mixed spinel. Though the charges of **A** and **B** in the prototypical spinel structure are +2 and +3 respectively, other combinations incorporating divalent, trivalent, or tetravalent cations, including (Mg, Zn, Fe, Mn, Al, Cr, Ti, and Si) are also possible. The anion is normally Oxygen.

Spinel ferrites exhibit ferromagnetic ordering. The magnetic moment of cations in the A-sites and B-sites are aligned parallel compared to one another. The arrangement is antiparallel between the A-sites and B-sites. Since there are twice as many B-sites as A-sites, there is a net moment of spins yielding ferromagnetic ordering. The selection of metal ions and the ion distribution between the A and B sites offer a tuneable magnetic system [2.22]. In NZF system, Ni^{2+} and Fe^{3+} are occupied in octahedral (B sites) and Zn^{2+} and Fe^{3+} are distributed in tetrahedral (A sites) in the lattice. The unit cell contains 32 O-atoms in cubic closest packing with 16 octahedral sites [2.23].

2.4 Perovskite Structure

Perovskite is any material with the same crystal structure of calcium titanium oxide ($CaTiO_3$) with the chemical formula ABO_3, where A and B are two cations with valences 2+ and 4+ respectively, O is oxygen anion that bonds both of them. The small cation B^{4+} is surrounded by an octahedron of 6-nearest neighbor O^{2-} (BO_6) and the large A^{2+} is coordinated with maximum 12-nearest neighbor O^{2-}. Such coordination form is stable if the sizes of A^{2+}, B^{4+} and O^{2-} vary under the limitation of famous Goldshmidt tolerance factor t [2.24]:

$$t = \frac{r_A + r_o}{\sqrt{2}(r_A + r_o)} \qquad (2.2)$$

The t factor somehow decides the lattice types of perovskite [2.25 - 2.26] t = 1 for a perfect cubic lattice. However, due to variation in ionic radii of various ions, many perovskites show deviations from t = 1 and may not even have a cubic structure. Deviations from t = 1 signify the level of lattice distortion.

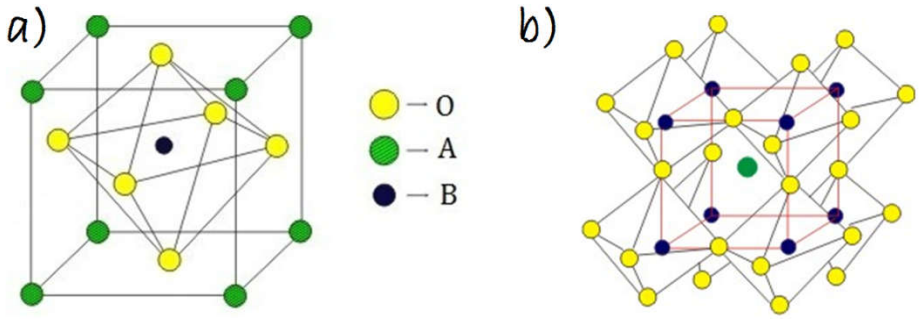

Figure 2.4: a) Perovskite structure b) Polyhedra model of perovskite structure

In $BiFeO_3$, Bi^{3+} ions take place in the A-site and Fe^{3+} ions in the B-site of the perovskite structure. The number of formula unit in perovskite structure is one.

2.4.1 Perovskite $BiFeO_3$

BFO is known to be the only single-phase ABO_3 type perovskite compound which possesses multiferroic properties at room temperature. In the crystal structure, Bi^{3+} ions are in the A-sites (corner) and Fe^{3+} ion takes place in the B-sites (centre) and O^{2-} ions take place in the middle of every surface.

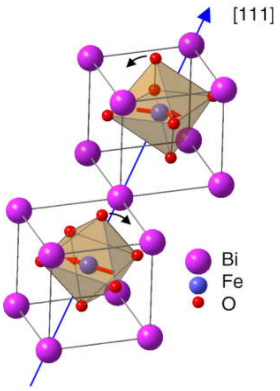

Figure 2.5: Crystal structure of bulk $BiFeO_3$

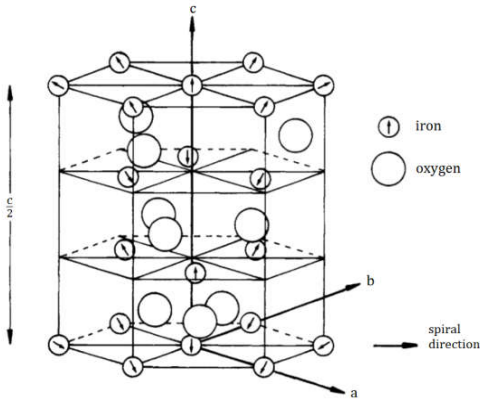

Figure 2.6: Hexagonal symmetry of $BiFeO_3$ lattice

Multiferroic, BFO exhibits both ferroelectric (below Tc = 830^0 C) and weak magnetic orders (below T_N = 370^0 C) simultaneously. It shows a rhombohedrally distorted perovskite structure with R3c space group ($a = 5.59\ A^0$ and $\alpha = 60.68^0$), and the unit cell of which can also be described in a hexagonal symmetry. At room temperature, the BFO is known to show antiferromagnetic G-type spin configuration along the pseudo cubic $[111]_c$ or rhombohedral $[001]_h$ direction while having a superimposed incommensurate cycloid spin structure with a periodicity of 620 Å along the $[110]_h$ axis, thus leaving only residual moments from canted spin structures to cause only weak magnetic properties [2.27].

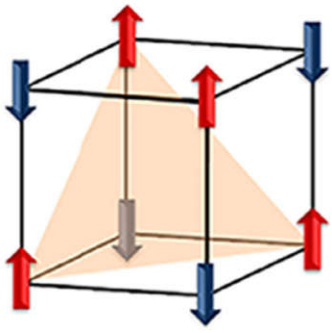

Figure 2.7: G-type antiferromagnetic Order

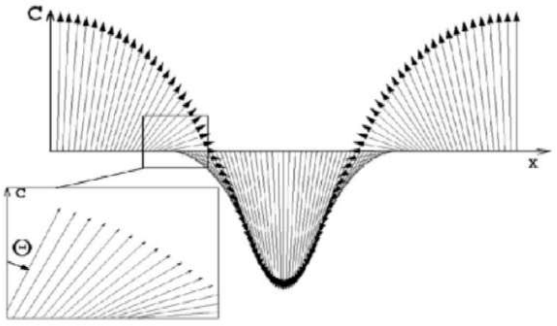

Figure 2.8: Schematic antiferromagnetic spin structure of $BiFeO_3$

The stereo chemical activity of the $6s^2$ lone pair electrons of the Bi^{3+} which are responsible for the FE while the magnetic properties are from partially filled d-orbital's of Fe^{3+} ions, indicating that the multiferroic nature of BFO is because of a non-d-electron mechanism for FE and a d-electron mechanism for magnetism.

2.5 Piezoelectrics

Piezoelectric Effect is the ability of certain materials to generate an electric charge in response to applied mechanical stress. It is understood as the linear electro-mechanical interaction between the mechanical and the electrical state in crystals. Piezoelectric effect is a reversible process means it exhibit the direct piezoelectric effect and the converse piezoelectric effect. When piezoelectric material is placed under mechanical stress, a shifting of the positive and negative charge centers in the material takes place, which then results in an external electrical field. When reversed, an outer electrical field either stretches or compresses the piezoelectric material.

2.5.1 Ferroelectricity and Ferroelectric Materials

Ferroelectricity is the phenomenon which refers to the state of spontaneous polarization, i.e., polarization of the material in the absence of an electric field. Materials exhibiting such property are called the ferroelectric materials. Though the prefix ferro is used, most ferroelectric materials do not contain iron [2.28]. In ferroelectric materials, the centers of positive and negative charges do not coincide with each other even in the absence of the field, thus producing a nonzero value of the dipole moment. The variation of polarization with electric field is not linear for such materials but forms a closed loop called hysteresis loop. Ferroelectricity disappears above a certain critical temperature called the Curie point (T_c) where the material gets transformed from ferroelectric to paraelectric state as indicated by a rapid decrease in the dielectric constant with the increase in temperature.

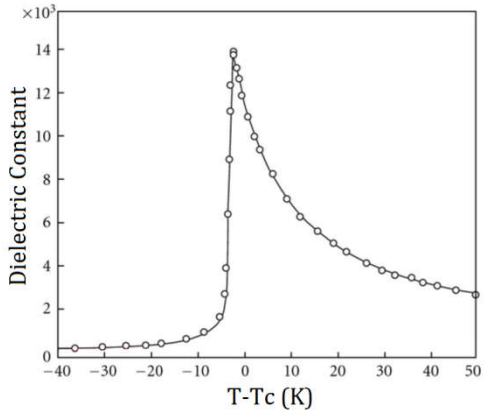

Figure 2.9: Temperature dependent dielectric constant of $BaTiO_3$

Different origins of ferroelectricity have been explored, such as charge ordering, magnetically induced ferroelectricity, lone-pair electron effects, octahedral distortion, strain mediation, geometrical frustration, etc., but in general, ferroelectricity results from relative shifts of negative and positive ions that induce surface charges; usually it requires formally empty d-orbital's.

Ferroelectric materials offer a wide range of useful properties. These include ferroelectric hysteresis for non-volatile memories, high permittivity for capacitors, high piezoelectric effect for sensors, actuators and resonant wave devices such as radio-frequency filters, high pyroelectric coefficients for infra-red detectors, strong electro-optic effects for optical switches and anomalous temperature coefficients of resistivity for electric-motor overload-protection circuits. In addition, ferroelectrics can be made in a wide variety of forms, including ceramics, single crystals, polymers and thin films – increasing their exploitability.

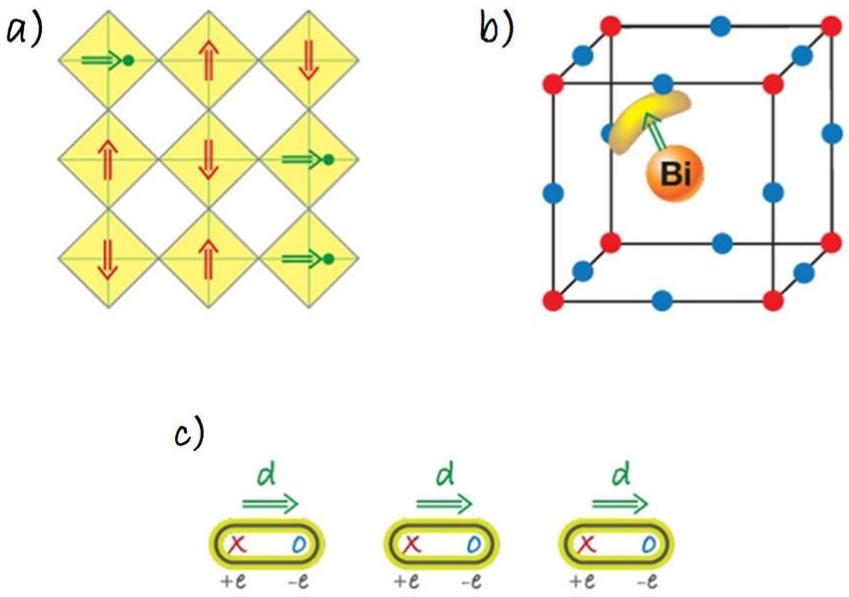

Figure 2.10: Different microscopic mechanisms of ferroelectricity (a) In 'mixed' perovskites with ferroelectrically active d^0 ions (green circles) and magnetic d^n ions (red), shifts of d^0 ions from the centers of O_6 octahedra (yellow plaquettes) lead to polarization (green arrows), coexisting with magnetic order (red arrows). (b) In materials like $BiFeO_3$ and the ordering of lone pairs (yellow "lobes") of Bi^{3+} and Bi^{3+} ions (orange), contributes to the polarization (green arrow). (c) In charge ordered systems, the coexistence of in equivalent sites with different charges, and in equivalent (long and short) bonds, leads to ferroelectricity.

2.6 Dielectrics

Dielectrics are basically electric insulators which ordinarily do not contain any free charge carriers for conduction but can be polarized by an applied electric field. When a dielectric is placed in an external electric field, it gets polarized and creates an internal electric field in the opposite direction, therefore reduces the overall field within the dielectric [2.29]. Materials which possess these properties are called dielectric materials which are a poor conductor of electricity, but efficient supporters of electrostatic field. This provides an exclusive property to the dielectric materials to be used as capacitor element.

Dielectrics are two in kinds:

(i) Polar dielectric.

(ii) Nonpolar dielectric.

Polar dielectrics are those in which centre of gravity of the positive and negative charges are separated by a finite distance (10^{-10} m). Thus, polar molecular or dielectrics have permanent dipole moment. Water, CO_2, NH_3 etc. are some examples of polar dielectrics. In case of non polar dielectrics the centers of both positive as well as negative charges coincide. Dipole moment of each molecule in non polar system is zero. All those molecules which belong to this category are symmetric in nature. Examples of non polar dielectrics are: methane, benzene etc.

2.6.1 Dielectric Polarization

Dielectric is placed in an external electric field, the positive and negative charges are displaced from their equilibrium positions by very small distances less than an atomic diameter throughout the volume of the dielectric. This results in the formation of a large number of dipoles each having some dipole moment in the direction of the field. The material is said to be polarized with a polarization defined as the dipole moment per unit volume of the material [2.30].

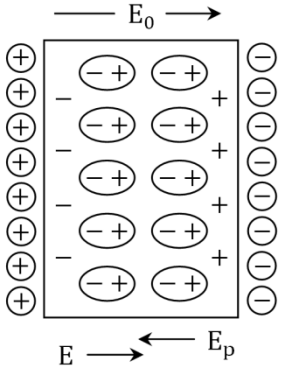

Figure 2.11: Schematic figure of a dielectric polarization

If the applied electric field is E_o and the polarized field within the dielectric is E_p then the overall electric field E can be defined as

$$E = E_o + E_p \tag{2.3}$$

The polarization field E_p tends to oppose the applied field E_o thus the resultant filed get reduced. For ordinary electric fields, the polarization P is proportional to the macroscopic field E. It is expressed as

$$P = \varepsilon_o \chi_e E \tag{2.4}$$

Where, ε_o is the permittivity of free space, χ_e is the electric susceptibility.

The electric susceptibility χ_e of a dielectric material is a measure of the polarization produced in the material per unit resultant electric field. This in turn determines the electric permittivity of the material and thus influences many other phenomena in that medium.

2.6.2 Dielectric Constant

Dielectric constant is defined as the ratio of the capacitance of a capacitor filled with a given dielectric to the capacitance of the same capacitor with vacuum. It is a number without dimensions, a quantity measuring the ability of a substance to store electrical energy in an electrical field. If C represents the capacitance of a capacitor with dielectric and C_0 represents the capacitance of the same capacitor with vacuum, then the dielectric constant (ε') can be given by

$$\varepsilon' = \frac{C}{C_o} \tag{2.5}$$

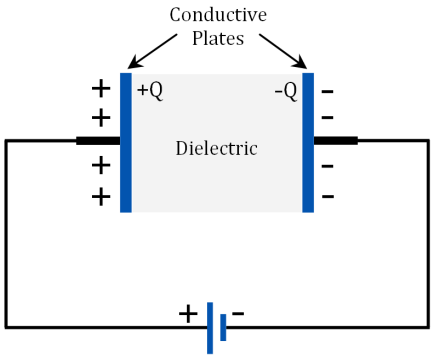

Figure 2.12: Schematic illustration of capacitive cell

But capacitance C of a parallel plate capacitor can be expressed as

$$C = \frac{\varepsilon A}{d} \tag{2.6}$$

Where, A is the area of each plate, d represents the separation between the plates and ε represents the permittivity of the dielectric material within the capacitor. If ε_0 represents the permittivity of the free space, then from equation (2.5) we get

$$\varepsilon' = \frac{\varepsilon}{\varepsilon_o} \tag{2.7}$$

Therefore, dielectric constant can also be defined as the ratio of the permittivity of a substance to the permittivity of free space. It is an expression of the extent to which a material concentrates electric flux, and is the electrical equivalent of relative magnetic permeability.

2.6.3 Dependence of Dielectric Constant on Frequency

Polarization systems respond to an electrical field by shifting their masses around and forms dipoles. These shifted masses are accelerated and de-accelerated with the change of the applied field which takes some time. Therefore, the polarization mechanism of a system depends on the frequency of the applied electrical field. Alternating electrical field induces alternating forces to the dipoles. Since the dipole response to a field involves the movement of masses, inertia will prevent the arbitrarily fast movements. When the frequency of the applied field increases, this movement of dipoles also increases. At high frequency, the dipoles are unable to cope with it. So at very high frequencies all movement of dipoles will 'die out' and there will be no response of the dipoles to the frequency field [2.31]. Dielectric constant (ε') is a measure of polarization of a system, it also depends on the frequency of the applied field. In general as frequency increases, its dielectric constant drops. But for some material the dielectric constant can increase with the increase in frequency due to the parasitic effect but only at the low temperature.

2.6.4 Dielectric loss

Dielectric loss is the portion of energy electric field in a dielectric medium that is converted into heat. When the value and direction of the applied field intensity change, the dielectric polarization also varies in value and direction. During one cycle of an alternating field the polarization is established twice and disappears twice. If the dielectric is made up of molecules that are dipoles themselves (polar molecules) or contain weakly bound ions the orientation or displacement of these particles in an electrical field is orientation polarization requires a definite relaxation time. As a result, the polarization maximum does not occur simultaneously with the maximum of

the filed intensity that is there is a phase shift between field intensity and polarization. Because of this there is also a phase difference between the field intensity and the electrical induction, which causes the energy loss [2.32]. Dielectric loss can be parameterized in terms of either the loss angle δ_E or the corresponding loss tangent $\tan\delta_E$. The electric loss tangent can be similarly defined as the ratio of the imaginary part of the permittivity (ε") to the real part of the permittivity (ε').

$$\tan \delta_E = \frac{\varepsilon''}{\varepsilon'} \tag{2.8}$$

A capacitor's loss tangent is sometimes stated as its dissipation factor or the reciprocal of its quality factor Q as follows

$$\tan \delta_E = \frac{1}{Q} \tag{2.9}$$

2.7 Temperature Dependence of Resistivity

The electrical resistivity of most materials changes with temperature. If the temperature *T* does not vary too much, a linear approximation is typically used as,

$$\rho(T) = \rho_o[1 + \alpha(T - T_o)] \tag{2.10}$$

Where, α is called the temperature coefficient of resistivity, T_0 is a fixed reference temperature usually room temperature, and ρ_o is the resistivity at temperature T_0. The parameter α is an empirical parameter fitted from measurement data. Because the linear approximation is only an approximation, α is different for different reference temperatures.

Temperature varies over a large temperature range, the linear approximation is inadequate and a more detailed analysis and understanding should be used. Metals have positive temperature co-efficient so resistance increases with temperature but in semiconductors it decreases with increasing temperature due to the presence of a negative temperature co-efficient. In case of insulator, resistivity also increases with temperature [2.33].

CHAPTER III

EXPERIMENTAL PROCEDURE

EXPERIMENTAL PROCEDURE

3.1 Methodology of Nanostructured Multiferroic Composites Preparation

Nanocrystalline materials have recently attracted a great scientific interest because of their unique properties and potential for advanced applications. Owing to constraint in nanometer scale (i.e., below 100 nm in at least one dimension) these materials exhibit a quantum confinement effect and hence differ in properties from their bulk counterparts. A bulk material should have constant physical properties regardless of its size, but at the nanoscale size-dependent properties such as quantum confinement in semiconductor particles, surface Plasmon resonance in some metal particles and super-paramagnetism in magnetic materials are often observed. Synthesis of nanoparticle is not an easy task. In fact it is a challenge, because controlling the particle size is a complex and durable work. Reduced particle size is not always desirable. For example, ferromagnetic materials smaller than 10 nm can switch their magnetization direction using room temperature thermal energy, thus making them unsuitable for memory storage [3.1].

3.1.1 Aspects of Present Work

In this research work, oxide materials in powder from were used to obtain multiferroic composites. To produced nanoparticle, conventional solid state reaction method with different dispersion techniques was used. In general, it is not familiar to synthesis nanoparticle with oxide materials, and there is no such cost effective technique to synthesis nanoparticle. From this motivation, conventional ceramic method aided with some mechanical approaches was used. Mechanical approaches were used to disperse particles from their neighboring particles which helped to confine the particle size in nanoscale. Conventional ceramic method was used to mix the powder where magnetic stirring and power ultrasonification was used to disperse the samples while centrifuge machine was used to wash the samples.

3.1.2 Problems with Conventional Methods

Though conventional ceramic method is a cost effective technique, it is an energy consuming monotonous process. The major drawback of this method is the

inhomogeneous mixing of the substance. The particle size distribution is also inhomogeneous. It is a 'top-to-bottom' method and the mechanical approaches which are needed to confine particle size in nanoscale are not much effective [3.2]. Another drawback is that, solids do not react together at room temperature over normal time scales and it is necessary to heat them to much higher temperature.

3.1.3 Reason of Using Oxide Materials

Obtaining nanoparticle in liquid state reaction method, like sol-gel method, chemical co-precipitation method etc. requires raw materials in acidic and alkali form which are costly. Moreover they require a solvent to defuse and react with each other. So there is a question of PH control, where one can easily be fused. But metallic oxides are the most cost effective and available materials which have been using in many purposes of scientific work. Unfortunately, obtaining nanoparticles from metallic oxides are not simplified from the view of synthesis mechanism. If it is possible to obtain nanoparticle from oxide materials where no chemical reaction is needed, then it will be a great achievement.

3.1.4 Selection of Raw Materials

As discussed in the previous chapters, this research work is designed to synthesis multiferroic composites. So it is very important to select novel ferroelectric and ferromagnetic materials which will satisfy the target of this research. BFO is highly popular as active ferroelectric material**,** where small addition of Europium improves its weak magnetic properties. Likewise NZF is well established ferromagnetic materials. It shows high electrical resistivity, high value of saturation magnetization, low eddy current losses. The large piezoelectric coefficient of BFO and high magnetostriction coefficient of NZF make them well-suited for preparing multiferroic composite and better ME coupling.

3.1.5 Weighing the Raw Materials at Precise Ratio

All the raw materials were collected with 99.99% purity and they were from Merck Aldrich and Sigma Aldrich Company. The raw materials were weighted in exact ratio in digital weight machine as shown in table 3.1. The materials were weighted with high sensitivity and preserved with extra care. So there was no chance to mix additional impurities in raw materials.

Table 3.1: Detail calculation of materials used in research

For $Bi_{0.9}Eu_{0.1}FeO_3$						
Content	Atomic mass(gm)	In 1 mole	Content	Atomic mass in the designed sample (gm)	In 20 gm of the sample	Atomic mass (gm)
Bi_2O_3	465.959	232.979	$0.9\_Bi_2O_3$	209.6815	$0.9\_Bi_2O_3$	13.6546
Fe_2O_3	159.688	79.844	Fe_2O_3	79.8441	Fe_2O_3	5.1995
Eu_2O_3	351.926	175.963	$0.1\_Eu_2O_3$	17.5963	$0.1\_Eu_2O_3$	1.1458
Total		488.786	**Total**	307.1219	**Total**	19.9996
For $Ni_{0.6}Zn_{0.4}Fe_2O_4$						
NiO	74.6928	74.6928	0.6_NiO	44.81568	0.6_NiO	3.78103
ZnO	81.3794	81.3794	0.4_ZnO	32.55176	0.4_ZnO	2.74634
Fe_2O_3	159.6882	79.8441	Fe_2O_3	159.6882	Fe_2O_3	13.47263
Total		235.9163	**Total**	237.05564	**Total**	20

The weight percentage of the oxides used in various samples were calculated by using the formula

$$\text{Weight \% of oxide} = \frac{\text{Molecular wt. of oxide} \times \text{required wt. of the sample}}{\text{Molecular weight of the designed sample}}$$

The chosen materials are Bi_2O_3, Eu_2O_3, Fe_2O_3, Ni_2O_3, ZnO, among of the materials except ZnO, others were in two moles by default in chemical formula. However, according to the weight % of oxide materials it is very important to take one mole from these which would confirm the exact ratio.

3.2. Mixed and Milled the Samples (Hand Milling)

The desired composition were prepared by mixing the constituent materials through had milling done by mortar and pestle. Hand milling depends on the solid state inter-diffusion between raw materials. Dry powder materials don't have sufficient moisture to mix, so to increase the degree of mixing it can be performed in a wet medium. Addition of acetone improves the mixing mechanism as high-quality wet ingredient. Milling time is very important for well mixing of the materials.

Figure 3.1: (a) Ceramic Mortar-pestle and (b)mortar-pestle for nano

In preparation of the proposed composites, the mother phases were first hand milled for 4 hours in ceramic mortar pestle. Then the mother phases were mixed according to the composite formula $(1-x)\cdot \mathrm{BEFO} + x\cdot \mathrm{NZF}$ with x = 0.0, 0.1, 0.3, 0.5, 0.7 and 1.0 and further milled for 2 hours. After dispersing in magnetic stirrer and ultrasonicator, all the dried samples were again milled for 30 minutes to produce the desired nanoparticles.

3.2.1 Stirred the Samples in Magnetic Stirrer

Magnetic stirrer is a laboratory device used to mix components to get homogeneous liquid mixtures. It employs a rotating magnetic field to spin an immersed stir bar and consequently stir the liquid solution. Magnetic stirrer can uniformly rotate a liquid solution over a long time scale to produce homogeneous mixing and removes the problems of manual stirring. The stir bars are typically coated in Teflon, which is chemically inert and do not contaminate or react with the rotating mixture. Due to its small size, a stirring bar can more easily be cleaned and sterilized than other stirring devices.

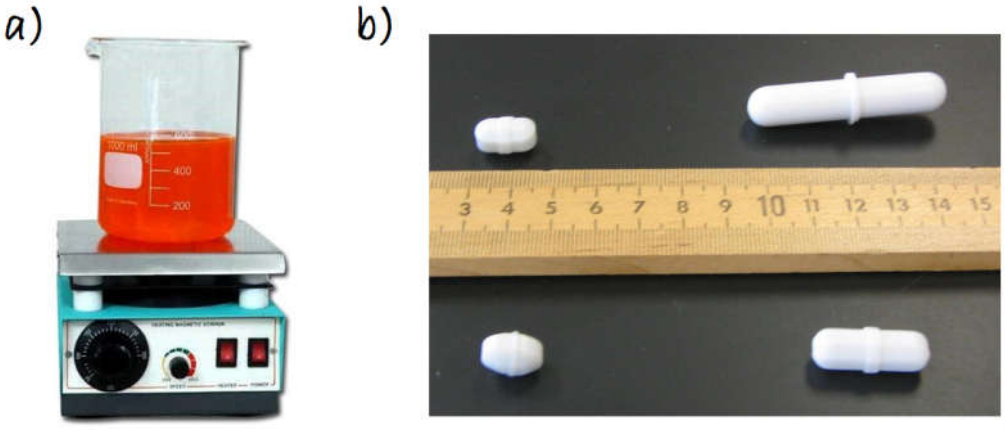

Figure 3.2: a) Magnetic stirring of oxide materials and b) different size of stirrer bars

To make a homogeneous mixture of BEFO and NZF powders, magnetic stirring was applied. As mixing substance, pure acetone and de-ionized water were used. Composite solution was made in a beaker with 30 ml acetone and was stirred gently with 360 rpm for 2 hours at room temperature. After 2 hours stirring the solution was kept at rest until the mixed materials get precipitated. Then acetone was removed carefully and washed in de-ionized water and again stirred for 10 minutes in de-ionized water. The uniform rotation of magnetic bar provides mechanical force to homogeneous mixing and disperses the neighboring particles.

3.2.2 Further Dispersion by Ultrasonicator

Sonication is the act of applying ultrasonic (> 20 KHz) sound waves to a liquid solution to agitate particles in that solution. Sound wave propagates into the solution with alternating high-pressure (compression) and low-pressure (rarefaction) cycles. When it contracts, negative pressure causes the liquid to flow up and while expanding it pushes the liquid. As liquids cannot flow as fast as the oscillation, during the contraction small vacuum cavities are formed. During the expansions, the cavities rapidly implode and create microscopic shock waves. This process is extremely powerful when the collective energy of all the imploding cavities is combined. The cavities are formed and collapse in microseconds which releases tremendous energy within the liquid causing their molecules to break apart [3.3].

Figure 3.3: Ultrasonic dispersion bath

In KUET solid-state lab, Hwashin power sonic bath was used to disperse the solution. It has a water chamber that must not be blanked or filled with water. The water level should be as high as the solution or to cover the maximum portion of the solution. A falcon tube with oxide samples dissolved in de-ionized water was putted on the water bath to vibrate for 20 minutes, and was repeated for 3 times. Here one

thing should be monitored that, during sonication the temperature of the water bath should not be raised over 30^0 C. After sonication, it was expected that a well mixed and dispersed solution had been obtained.

3.2.3 Centrifugation

Centrifugation is a technique used for separating particles from a solution according to their size, shape and density. Separation of solid particles from a solution could be done through sedimentation naturally with the earth gravity, but it would take a long time. Centrifugation makes that natural process much faster. A centrifuge device contains centrifuge tubes placed in a rotor, which rotates about a central axis. As a rotor spins, it produces a centrifugal force upon the particles in a solution. The particles then sediment at the rate proportional to the centrifugal force applied to it. At a fixed centrifugal force the sedimentation rate is proportional to the particle size and to the difference between the particle density and the density of the solution [3.4].

Figure 3.4: A four chamber centrifuge machine

A very important thing to be assured that, the centrifuge machine must be operated at balance state. This force imbalance strains the spindle and may results in damaging the centrifuge or personal injury. So the centrifuge machine should be carefully balanced. In Atomic Energy Centre, Dhaka, Eppendorf Centrifuge with 4 centrifuge chambers was used as the solution carrier. After balancing, the centrifuge was operated at 3000 rpm for 10 minutes. To prevent accident, the main lid was locked during the run. The effect of high rpm caused the solid particles precipitating at the bottom of the tube and the

water carried all other impurities with it. After 10 minutes the centrifuge was automatically stopped and the water was removed manually. To clean the samples effectively, the whole procedure was repeated for four times. After 4 times centrifuge wash the sediment was collected by a thin spun.

3.2.4 Drying the Samples in a Microwave Oven

Microwave oven is a device producing heat by electromagnetic radiation in the microwave frequency range. It is an efficient way to heat wet solution to dry without contamination. After centrifugation, all the samples were heated at 150^0 C in a microwave oven for 2 hours to dry the washed samples. That low temperature was not able to change the particle size or to create any phase change. The dried samples were in the lump form and were grounded into powder by agate mortar and pestle.

3.3 Pressing to Desire Shapes

In this stage, the pre-sintered powders were compacted into disk or toroid shape through the application of high pressures. The powder samples were first mixed with an organic binder PVA and then pressed into desired shapes. 1gm sample was used for preparing toroid and 0.5 gm sample was used for preparing disk. To prepare the toroids and disks, about 10 MPa and 15 MPa pressure was applied respectively.

Figure 3.5: Hydraulic press in solid-state lab of KUET and the prepared samples

3.4 Annealing

Annealing in metallurgy is a heat treatment that alters the physical and sometimes chemical properties of a material to increase its ductility and reduce its hardness. In annealing, atoms migrate in the crystal lattice and the number of dislocations decreases, leading to the change in ductility and hardness.

Figure 3.6: Furnace used in solid-state lab of KUET

In scientific terms, annealing is used to bring a metal closer to its equilibrium state. It involves heating a material above of its recrystallization temperature and then performing slow-cooling, usually by allowing it to cool in the furnace. In the present work, all the powder samples were annealed at 300^0C, 450^0C and 600^0C to observe the effect of heat on the grain growth.

3.5 Sintering

Sintering is a heat treatment applied in powder metallurgy to impart strength and integrity. In sintering process, one should mill the material to obtain fine grind powder, press it into a mould using a binder like PVA to stick it together and then heat inside a furnace. At sintering temperature, diffusion processes cause necks to form and grow at the contact points to convert the particles into a solid piece.

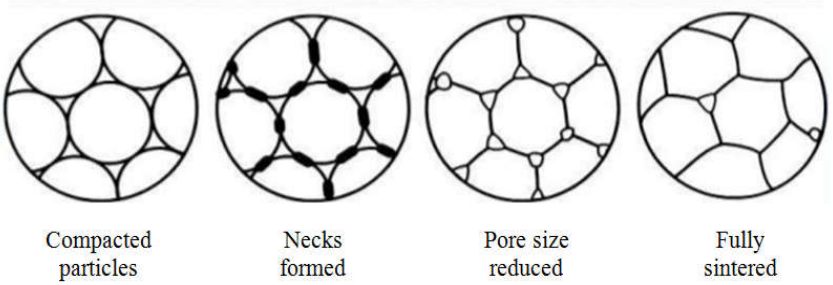

Figure 3.7: Sintering on a microscopic scale: (a) particle bonding is initiated at contact points; (b) contact points grow into ‘necks’; (c) the pores between particles are reduced in size; (d) grain boundaries develop between particles in place of the necked regions

There are two necessary precursors before this 'solid state sintering' mechanism.

1. Removal of the pressing lubricant by evaporation and burning of the vapors.
2. Reduction of the surface oxides from the powder particles in the compact [3.5].

Sintering is effective to reduce the porosity and enhance properties such as strength, electrical conductivity, and thermal conductivity. In this work, all the disks and toroids were sintered at 850^0C to obtain workable samples of the composites.

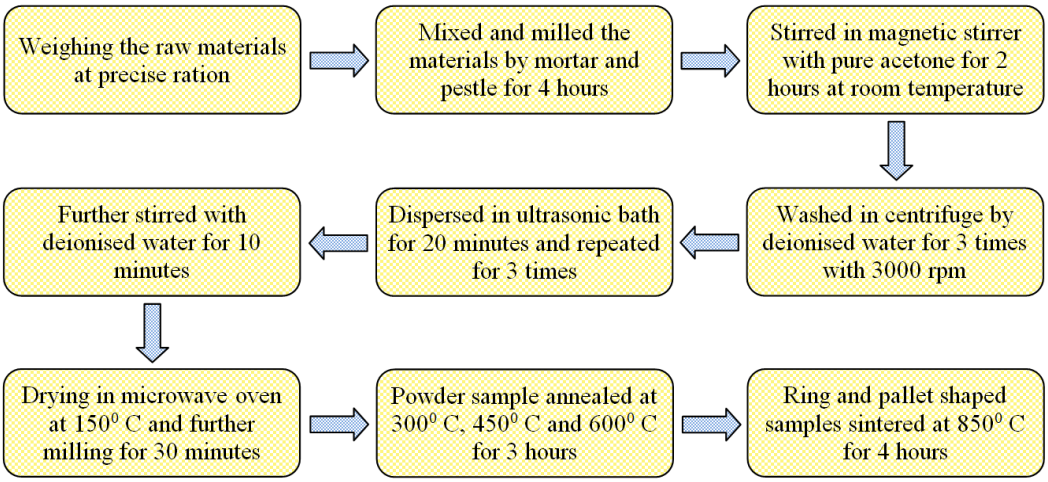

Figure 3.8: Flow chart of the sample preparation steps

3.6 X-ray Diffraction (XRD)

X-ray diffraction (XRD) is a rapid analytical technique primarily used for phase identification of a crystalline material and can provide information on unit cell dimensions. It provides precise knowledge of the lattice parameter as well as the substantial information on the crystal structure of the material under study.

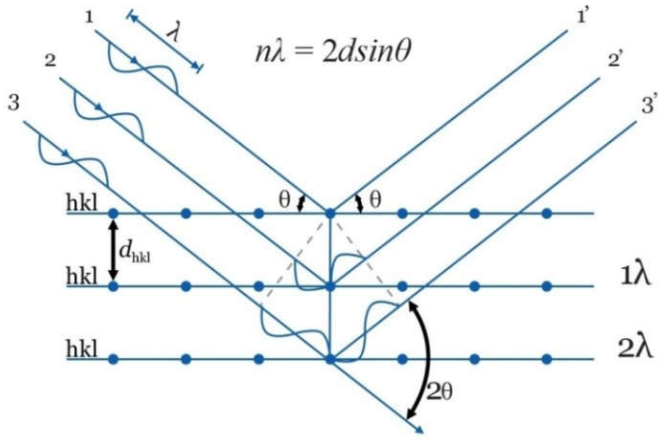

Figure 3.9: Bragg diffraction of x-rays from successive planes of atoms

XRD is based on constructive interference of monochromatic X-ray diffraction from a crystalline sample where crystalline substances act as three dimensional diffraction gratings with grating constant equal to the spacing of planes in the crystal lattice. The interaction of the incident X-rays with the sample produces constructive interference when satisfying the Bragg's condition:

$$2d \sin \theta = n\lambda \qquad (3.1)$$

This law relates the wavelength of electromagnetic radiation to the diffraction angle and the lattice spacing in a crystalline sample. Typically, this is achieved by comparison of d-spacing's with standard reference patterns [3.6].

3.6.1 Different Parts of the PHILIPS X'Pert PRO XRD System

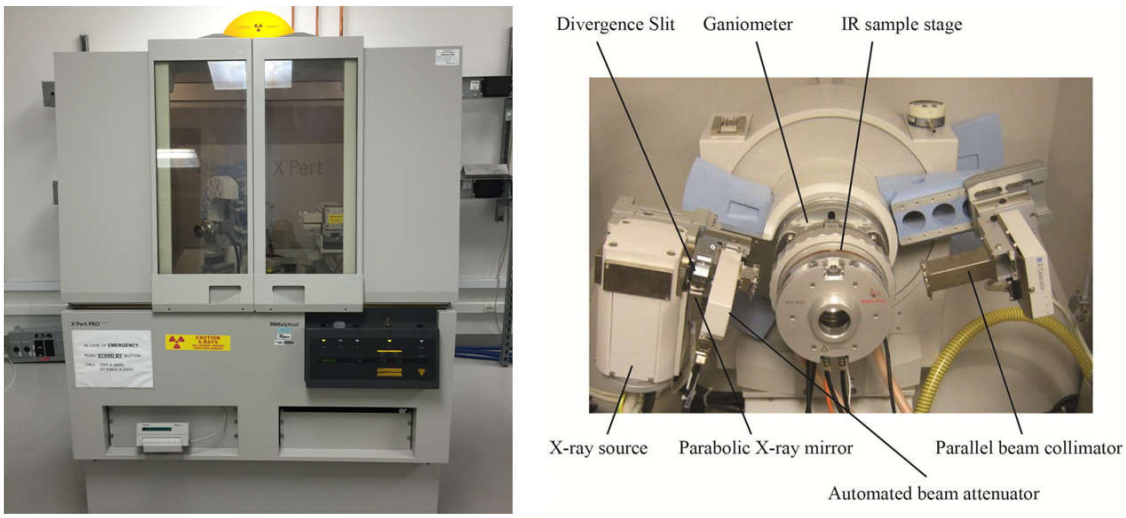

Figure 3.10: Internal arrangement of a PHILIPS X'Pert PRO X-ray diffractometer

In this research, Phillips X'pert PRO X-ray diffractometer of Atomic Energy Centre, Dhaka was used. The wavelength of the used X-ray is (λ = 1.5418 Å) and is of the same order of magnitude as that of the lattice constant of crystals and this makes it so useful in structural analysis of crystal structure.

3.6.2 Interpretation of the XRD Data

The XRD data consists of θ_{hkl} and d_{hkl} values corresponding to the different crystallographic planes and are used to determine the structural information of the samples like lattice parameters and constituent phases. We determine the inter-planar spacing 'd' from the Bragg's law.

$$2d_{hkl} \sin \theta = \lambda \qquad \text{i.e.,} \quad d_{hkl} = \frac{\lambda}{2 \sin \theta}$$

Where λ is the wavelength of the X-ray, θ is the diffraction angle and n is an integer representing the order of the diffraction and h, k, l are the miller indices.

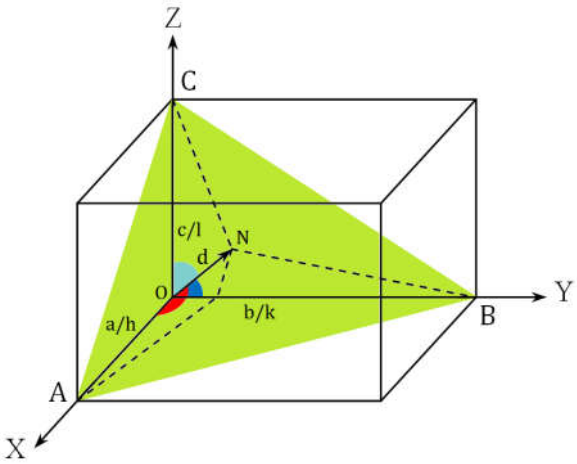

Figure 3.11: Crystal plane orientation

From the figure,

$$\cos^2\alpha + \cos^2\beta + \cos^2\gamma = 1 \qquad (3.2)$$

But, $\angle ONA = \angle ONB = \angle ONC = 90°$

Now, from right angle triangle ΔAON, we can write . . .

$$\cos\alpha = \frac{ON}{OA} \qquad \Rightarrow ON = OA\cos\alpha$$

$$\text{or,} \quad d = \frac{a}{h}\cos\alpha \qquad \Rightarrow \cos\alpha = \frac{dh}{a}$$

$$\text{similarly,} \quad \cos\beta = \frac{dk}{b} \quad \text{and} \quad \cos\gamma = \frac{dl}{c}$$

Now substituting the values of $\cos\alpha$, $\cos\beta$ and $\cos\gamma$ in equation (3.2) we have

$$d^2\left[\frac{h^2}{a^2} + \frac{k^2}{b^2} + \frac{l^2}{c^2}\right] = 1 \qquad \text{or,} \quad \frac{1}{d^2} = \left[\frac{h^2}{a^2} + \frac{k^2}{b^2} + \frac{l^2}{c^2}\right]$$

For cubic lattice with a=b=c, this equation becomes,

$$d^2 = \frac{a^2}{h^2 + k^2 + l^2} \qquad (3.3)$$

For other types of lattice equation (3.3) becomes

$$\frac{1}{d^2} = \frac{4(h^2 + hk + k^2)}{3a^2} + \frac{l^2}{c^2} \qquad \text{(For rhombohedral)}$$

$$\frac{1}{d^2} = \frac{h^2}{a^2} + \frac{k^2}{b^2} + \frac{l^2}{c^2} \qquad \text{(For orthorhombic)}$$

$$\frac{1}{d^2} = \frac{h^2 + k^2}{a^2} + \frac{l^2}{c^2} \qquad \text{(For tetrahedral)}$$

Now substituting for d in equation (3.1) and square both sides we have

$$4a^2\sin^2\alpha = n^2\lambda^2(h^2 + k^2 + l^2)$$

$$\text{or, } \sin^2\alpha = \frac{n^2\lambda^2}{4a^2}(h^2 + k^2 + l^2) \quad (3.4)$$

There are a very simple relation between miller indices and crystal structures [3.7].

Table 3.2: Relationship between Bravais lattice and reflections

Crystal Structure	Planes present in Diffraction	Planes absent from diffraction
Simple Cubic	All h, k, l	None
FCC	h, k, l all odd or all even	h, k, l mixed (not all odd or all even)
BCC	h + k + l = even	h + k + l = odd
Base-centred	h and k both even or both odd *	h and k mixed *
Hexagonal close-packed	h + 2k = 3N with l even h + 2k = 3N ± 1 with l odd	h + 2k = 3N with l odd h + 2k = 3N ± 1 with l even

* These relations apply to a cell, centered on the C face. If reflections are present only when h and k are unmixed, or when k and l are unmixed, then the cell is centered on the B or A face, respectively.

This is essentially Bragg's condition for cubic crystals. It indicates that angle increases with ($h^2 + k^2 + l^2$) and higher order Miller indices give rise to wider diffraction angles. The Bragg's law for cubic crystals in equation (iv) is a necessary diffraction condition but not sufficient because diffraction involves the interaction of EM waves with the electrons in the crystals. Though the full theoretical analysis is beyond the scope of this paper, the results are nonetheless straightforward and useful. Table-3.2 lists the conditions for the presence and absence of peaks from various planes in cubic crystal structures [3.8].

3.6.3 X-ray Density and Bulk Density

Bulk density is defined as the dry mass of particles of the material divided by the total volume they occupy. The total volume includes particle volume, inter-particle void volume and internal pore volume.

$$\text{Bulk density } \rho_b = \frac{\text{mass of solid}}{\text{volume as a whole}} = \frac{M_s}{V_t} = \frac{m}{\pi r^2 h} \quad (3.5)$$

Where m is the mass of the sample, r is the radius and h is the thickness of the pellet. X-ray (also known as particle density) density ρ_x of a sample can be estimated by using the following relation that suggested by Smith and Wijn

$$\rho_x = \frac{n\,M}{N_A V} \tag{3.6}$$

Where, 'n' denotes the number of formula unit per unit cell (in perovskite structure n = 1 and in spinel structure n = 8), M indicates the molar mass of the sample, N_A is the Avogadro's number (6.02×10^{23} mol^{-1}) and V is the volume of the unit cell [3.9].

3.6.4 Porosity

Determining the porosity of a composite material is little bit tricky, because it consists of independent phases of different molecular weight with different quantity and X-ray density. Here, the composite material has formula (1x) $[Bi_{0.9}Eu_{0.1}FeO_3]$ + x$[Ni_{0.6}Zn_{0.4}Fe_2O_4]$ with x = 0.0, 0.1, 0.3, 0.5, 0.7 and 1.0. The X-ray density of BEFO and NZF are

$$\rho_{x\,(BEFO)} = \frac{nM_{BEFO}}{N_A V_1} \qquad \text{and} \qquad \rho_{x\,(NZF)} = \frac{nM_{NZF}}{N_A V_2}$$

n=6 for BEFO for having perovskite structure and n=8 for NZF having spinel structure. V_1 and V_2 are the unit cell volume of BEFO and NZF respectively.

If BEFO and NZF have X-ray volume V_{1x} and V_{2x} respectively, then

$$V_{1x} = \frac{M_{BEFO}}{\rho_{x\,(BEFO)}} \qquad \text{and} \qquad V_{2x} = \frac{M_{NZF}}{\rho_{x\,(NZF)}}$$

Then the X-ray density of the composite materials should be

$$\rho_{x\,(composite)} = \frac{M_1 + M_2}{V_{1x} + V_{2x}}$$

Where, M_1 is the (1-x) times molecular weight of BEFO and M_2 is the 'x' times molecular weight of NZF.

Therefore, porosity of the composite can be given by

$$\text{Percent porosity} = \left(1 - \frac{\rho_b}{\rho_x}\right) \times 100\% \tag{3.7}$$

Where ρ_b is the bulk density determined by equation (v) [3.10].

3.6.5 Crystalline Size

The Scherrer equation in X-ray diffraction and crystallography is a formula that relates the size of sub-micrometre particles, or crystallites, in a solid to full width half maximum of a peak in a diffraction pattern. It is named after Paul Scherrer and can be written as:

$$D = \frac{k\lambda}{\beta \cos\theta} \qquad (3.8)$$

Where, D is the mean size of the crystalline domain, which may be smaller or equal to the grain size. K is a dimensionless shape factor, with a typical value of about 0.9. λ is the X-ray wavelength. β is the full width half maximum of the XRD peak. θ is the Bragg angle.

3.7 Field Emission Scanning Electron Microscope (FESEM)

Field emission scanning electron microscope (FESEM) is a powerful version of a scanning electron microscope. It provides topographical and elemental information at magnifications of 10x to 300,000x, with virtually unlimited depth of field. It uses a beam of electrons shot towards a sample to obtain information about it, including what the surface looks like and the chemicals make up of the sample.

Figure 3.12: Field Emission Scanning Electron Microscope (FESEM)

The surface morphology and nano structured particle size of the prepared sample was studied by FESEM (JEOL JSM 7600F) from Glass & Ceramic Engineering Department of Bangladesh University of Engineering and Technology, Dhaka, Bangladesh. For FESEM measurement, powder sample that sintered at 850^{o}C for 4 hours were used.

3.8 Vibrating Sample Magnetometer (VSM)

A vibrating Sample Magnetometer (VSM) is a scientific instrument to measure the magnetization of a sample under an external magnetic field. It operates on the Faraday's low of induction.

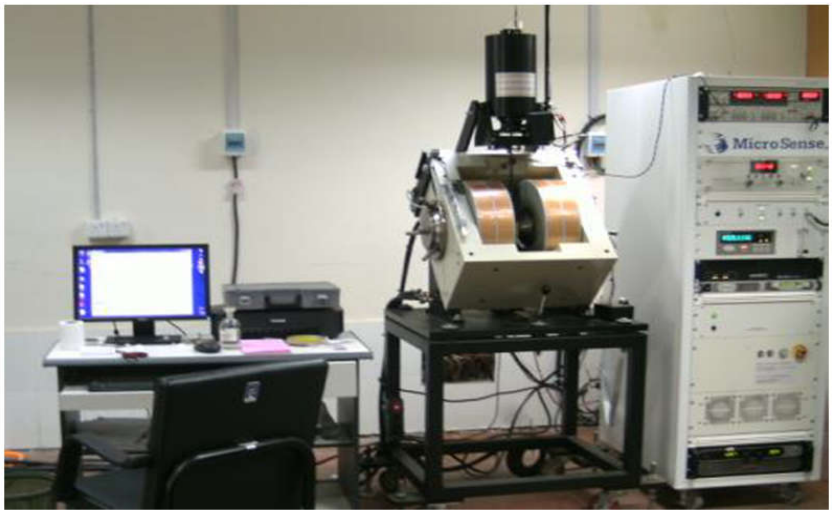

Figure 3.13: MicroSense Vibrating Sample Magnetometer

The working principle of VSM is the measurement of the electromotive force induced by a magnetic sample when it is vibrated at a constant frequency in the presence of a static and uniform magnetic field. In a VSM, a sample is placed within a uniform magnetic field H which induces a magnetization M in the sample. It is then vibrated sinusoidally, which creates a corresponding vibration of the magnetic flux in the pick-up coils nearby and induces a sinusoidal voltage. The amplitude of the ac voltage is proportional to the samples magnetic moment and measured by a lock-in amplifier [3.11].In this study, Microsense VSM model EV7 at Atomic Energy Commission, Dhaka was used to determine the magnetic properties of the samples. A small part of the samples (9 -11 mg) were used and was made to avoid movements inside the sample holder. To understand the ferromagnetic effect, full-cycle hysteresis loops were obtained over a wide range of field from -10 KOe to +10 KOe.

3.9 Frequency Characterization of the Present Samples

For high frequency application, the desirable property of a material is high permeability with low loss. One of the most important goals of material research is to fulfill this requirement. The techniques of permeability measurement and frequency characteristics of the present samples are described in the following way.

3.9.1 Electric and Dielectric Measurements

Frequency dependence of AC resistivity of the prepared samples were measured using conventional two probe method using pellet samples sintered at 850^0 C. The samples were polished using 400 degree emery paper and then cleaned with

acetone. Two copper wire of 0.01 mm diameter were added on both sides of the pellet samples through silver paste for conduction.

Figure 3.14: Wayne Kerr Impedance analyzer 6500B at solid-state lab KUET

The frequency dependent dielectric constant and resistance had been measured as a function of frequency ranging from 1 KHz to 12 MHz at room temperature by the Wayne Kerr 6500B Impedance Analyzer at solid-state lab KUET. It can automatically measure the inductance (L), capacitance (C) and resistance (R) and other parameters such as the quality factor, impedance, AC resistance, conductance and dielectric loss tangent of the subjected materials with 0.05% accuracy.

The dielectric parameters were evaluated by using the relations given below,

$$\varepsilon' = \frac{C}{C_0} = \frac{CL}{\varepsilon_0 A} \tag{3.9}$$

$$\varepsilon'' = \varepsilon' \cdot \tan\delta_E \tag{3.10}$$

Here, ε' and ε" are the real and imaginary part of the dielectric constant. C is the capacitance of the pellet samples in farad and C_0 is the capacitance of the capacitor without the dielectric materials. $C_0 = \frac{\varepsilon_0 A}{L}$, and can be derived theoretically. ε_0 is the permittivity of the free space ($\varepsilon_0 = 8.854 \times 10^{-12}$ Fm^{-1}) and $A = \pi r^2$ is the cross sectional area of the pellet shaped sample.

Again, Quality Factor

$$Q = \frac{1}{\tan\delta_E} \tag{3.11}$$

And relative quality factor

$$RQF = \frac{\varepsilon'}{\tan\delta_E} \tag{3.12}$$

3.9.2 Complex Permeability Measurements

To determine the frequency dependent complex permeability of the studied samples, toroid shape samples were used. The polished samples were cleaned with acetone and then coiled with copper wire. The measurements of complex permeability of the toroid shaped samples were performed at room temperature in the frequency range from 1 KHz to 100MHz. The real part, μ' and imaginary part, μ" of the complex permeability were measured using the following formulas

$$\mu' = \frac{L_S}{L_0} \tag{3.13}$$

and $$\mu'' = \mu' \cdot \tan\delta_M \tag{3.14}$$

Here, L_S is the inductance of the sample and $L_o = \frac{\mu_0 N^2 S}{\pi \bar{d}}$ derived theoretically for the samples. L_0 is the inductance of the winding coil except the sample, N represents the number of turns of the coil (N = 5), S indicates the cross sectional area of the toroid samples as given below,

$$S = d \times h \tag{3.15}$$

and, $$d = \frac{d_2 - d_1}{2} \tag{3.16}$$

Where, d_1 is the inner radius, d_2 is the outer radius and h is the height of the ring. Again, $\bar{d}$ indicates the mean diameter of the toroidal sample and can be written as,

$$\bar{d} = \frac{d_1 + d_2}{2} \tag{3.17}$$

Again, Quality Factor

$$Q = \frac{1}{\tan\delta_M} \tag{3.18}$$

And relative quality factor

$$RQF = \frac{\varepsilon'}{\tan\delta_M} \tag{3.19}$$

3.9.3 Impedance Analysis

Electrical impedance is the measure of the opposition that a circuit presents to a current when a voltage is applied. Impedance extends the concept of resistance to AC circuits, and possesses both magnitude and phase, unlike resistance, which has only magnitude.

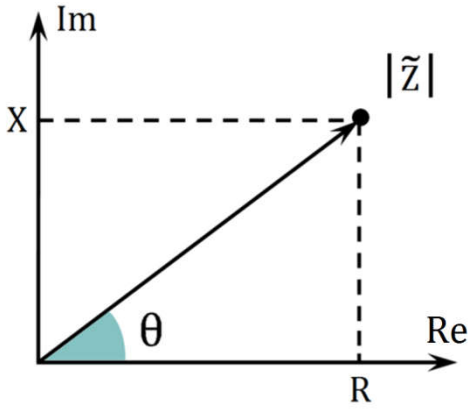

Figure 3.15: The real and imaginary part of impedance with resistance variance

For a sinusoidal current or voltage input, the polar form of the complex impedance relates the amplitude and phase of the voltage and current. In particular:

- The magnitude of the complex impedance is the ratio of the voltage amplitude to the current amplitude.
- The phase of the complex impedance is the phase shift by which the current lags the voltage [3.13].

The impedance of a two terminal circuit is a complex quantity and denoted by Z. In Cartesian form, impedance Z can be written as follow,

$$Z = R + jX \tag{3.20}$$

Where the real part R is the resistance and

$$R = \omega L_0 \mu'' \tag{3.21}$$

The imaginary part X is the reactance and,

$$X = \omega L_0 \mu' \tag{3.22}$$

Here ω represents the angular frequency. L_0 is the inductance of the circuit with air. μ' and μ'' are the real and imaginary part of the complex permeability.

CHAPTER IV

RESULTS AND DISCUSSION

RESULTS AND DISCUSSION

4.1 X-ray Diffraction Analysis

X-ray diffraction (XRD) analysis was carried out by using Philips X'pert PRO X-ray diffractometer (PW3040) equipped with CuK_{α} radiation (λ = 1.5418 Å). Powder samples annealed at 850^0 C for 3 hours were used to obtain the XRD patterns. The obtained XRD patterns of individual europium doped bismuth ferrite (BEFO), nickel zinc ferrite (NZF) phases along with the $(1-x)\cdot BEFO + x\cdot NZF$ composites have been shown in figure 4.2. The 2θ values and the corresponding peak intensity in the XRD patterns are well matched with the International Centre for Diffraction Data (ICDD) value and have been indexed with their corresponding Miller indices as reported for BEFO [4.1] and NZF [4.2] phases. It reveals that the ferroelectric BEFO phase exhibits distorted rhombohedral perovskite structure and the ferrite NZF phase exhibits the spinel cubic structure.

4.1.1 The Perovskite BEFO Phase

The XRD pattern of BEFO phase has shown in figure 4.2 with x = 0.0. The peaks have been indexed as (012), (104), (110), (202), (204), (116), (214) and (208), comparing with the previous works and the ICDD value [4.1]. There are no residual components and impurity phases found in the XRD pattern suggesting the successful incorporation of Eu into the BEFO lattice. A secondary impurity phase has been found around 2θ = 27.89^0 as indicated by (∗) and attributed to the kinematics of phase formation and to the partial volatilization of Bi under the employed sintering temperature and schedule. The lattice parameter has been calculated by using the formula $\frac{1}{d^2} = \frac{(h^2+hk+k^2)}{a^2} + \frac{l^2}{c^2}$ and got the value a = 5.5505 (Å) and c = 13.71936 (Å) which is in good agreement with the earlier reports [4.3]. The prominent XRD peaks are found in splitted form indicating the reduced structural symmetry of atoms in the BEFO lattice and indicating the distortion present in the phase.

4.1.2 The Cubic NZF Phase

The XRD pattern of NZF phase has been shown in figure 4.2 as x = 1.0. The strongest reflection peak has been found at 2θ value around 35^0 and assigned to (311)

diffraction plain typical for the spinel phase. All the 2θ values and their corresponding peak intensity are well matched with the ICDD value and the reflection peaks were identified and indexed in good agreement with the referred database of the ICDD [4.4]. The XRD spectra were indexed as (111), (220), (311), (400), (422), (511), (440) and (533) and fcc cubic phase has been identified as major phase. An impurity peak has been observed around ($2\theta = 31.8901^0$) and correspond to k_β contribution of (311) peak [4.5]. The lattice parameter of the NZF phase was calculated using the formula $a = d\sqrt{h^2 + k^2 + l^2}$. The calculated lattice parameter has the value a = 8.378 (Å) which is in good agreement with the previous reports [4.6]. The most prominent (311) peak is found in super-structural form as shown in figure 4.1 referring the undistorted lattice structure of the NZF phase.

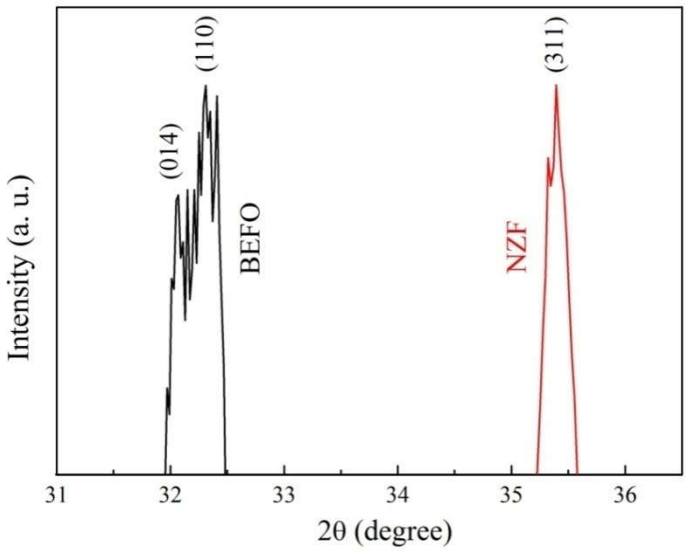

Figure 4.1: Comparison between the prominent peak of BEFO and NZF phase

4.1.3 The Composite Phase

The XRD patterns of $(1 - x) \cdot \mathrm{BEFO} + x \cdot \mathrm{NZF}$ composites with x values of 0.1, 0.3, 0.5 and 0.7 are shown in figure 4.2. It is observed from XRD spectra that the composites exhibit both the ferrite (NZF) and ferroelectric (BEFO) phases together. The intensity and number of the XRD peaks of the mother phases in the composites depend on the amount of corresponding phases in the composites. It can be noticed from the figure 4.2 that the intensity of the peaks corresponding to ferrite phase increases with increasing ferrite composition while that of the perovskite peaks decreases. No third phase has been observed in the XRD spectra confirms that there is no chemical reaction between the two phases.

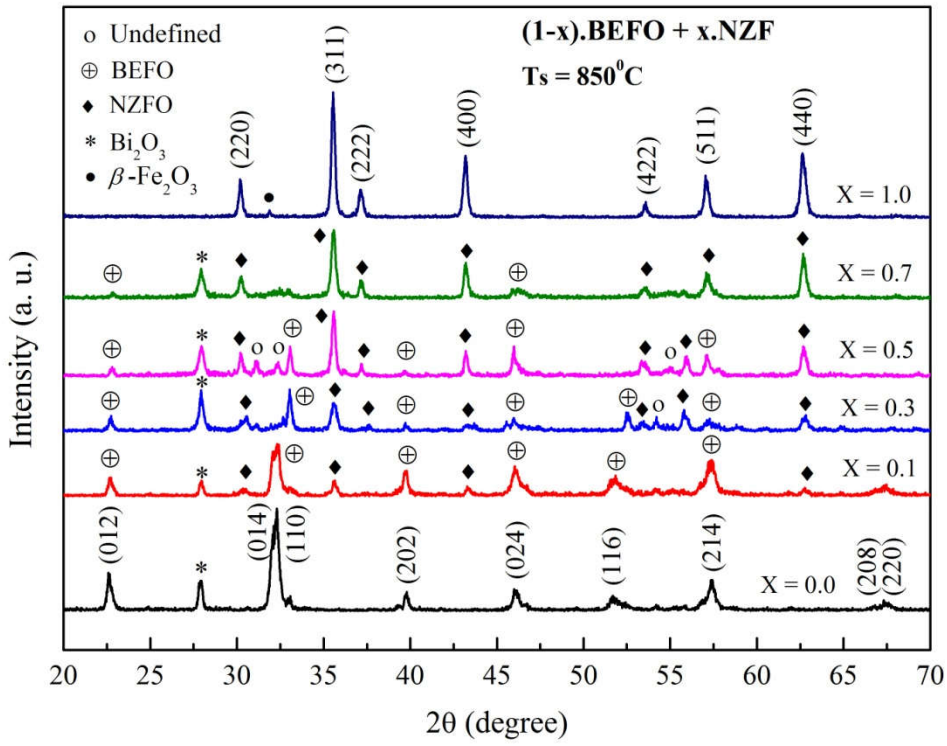

Figure 4.2: X-ray diffraction pattern of $(1-x)\cdot BEFO + x\cdot NZF$ composites with x = 0.0, 0.1, 0.3, 0.5, 0.7 and 1.0 sintered at 850^0 C

The calculated lattice parameter for both the ferrite and ferroelectric phases are given in table 4.1 and are good agreement with the earlier reports [4.7 - 4.8]. It is observed that in case of composites there is an insignificant change in the lattice parameter of ferroelectric and ferrite phase which may be due to stress exerted on each other by the two phases [4.9] and also due to the diffusion of a small amount of un-reacted elements into the two phases. The calculated bulk density (ρ_b), x-ray density (ρ_x) and porosity P are presented in table 4.1.

Table 4.1: The bulk density, X-ray density, porosity and lattice constant of various $(1-x)\cdot BEFO + x\cdot NZF$ multiferroic composites

Content (x)	Lattice parameters (Å)			ρ_b gm/cm^{-3}	ρ_x gm/cm^{-3}	P (%)
	BEFO		NZF			
	a	c	a			
0.0	5.551	13.719	-	6.5449	8.3597	21.71
0.1	5.549	13.723	8.353	6.7004	8.0051	16.29
0.3	5.529	13.674	8.353	6.1168	7.3368	16.63
0.5	5.635	13.753	8.369	5.4203	6.7183	19.32
0.7	5.583	13.772	8.373	4.9035	6.1440	20.19
1.0	-	-	8.378	2.7118	5.3558	49.37

Figure 4.3 shows the variation of ρ_b, ρ_x and P as a function of ferrite content sintered at 850 °C. The ρ_x decreases linearly with NZF content because ρ_x of NZF phase is less than that of BEFO phase. The ρ_b of $(1-x)\cdot \mathrm{BEFO} + x\cdot \mathrm{NZF}$ composites initially increases with NZF content (up to x = 0.1) which can be attributed to the small grain size of NZF phase, which fills the pores of BEFO phase. After x = 0.1 the ρ_b decreases with NZF content due to the lower ρ_b of NZF phase. The variation of porosity (P) with NZF follows the opposite trend of ρ_b which is first decreased and then increased with NZF content and becomes maximum for x = 1.0. Here, an extremely high porosity (49.37%) has been observed for x = 1.0 and can the attributed to the applied sintering temperature and schedule. In this work the sintering temperature was fixed at 850^0C which is quiet low for NZF to crystallize effectively with melting point around 1200^0C. Therefore the NZF phase has not crystallized comparing the other counterparts which results in the high porosity.

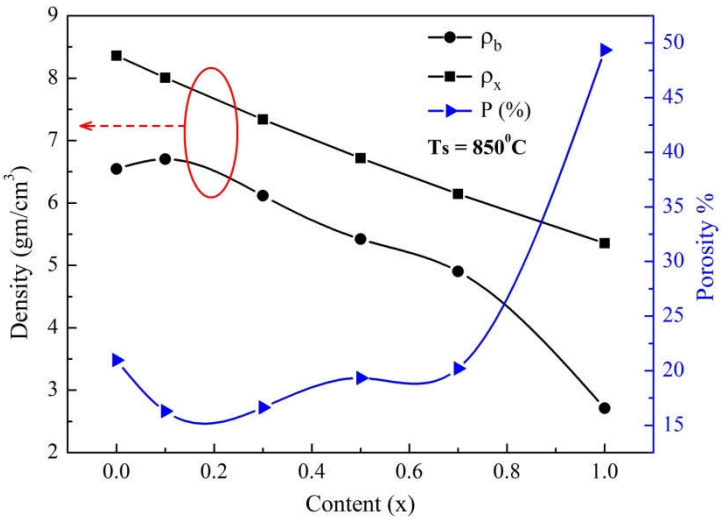

Figure 4.3: The ρ_x, ρ_b and porosity P as a function of ferrite content for various $(1-x)\cdot \mathrm{BEFO} + x\cdot \mathrm{NZF}$ composites sintered at 850^0 C

4.2 Confirmation of Nanostructure

One goal of the present study is to obtain nanoparticles by the proposed synthesis mechanism. Field Emission Scanning Electron Microscopy (FESEM) was used to observe the particle size and surface morphology of the prepared samples. Powder samples heated at 600^0 C for 2 hours were used to obtain FESEM micrographs. In the FESEM micrographs the agglomeration of fine grains with sharp grain boundaries have been observed. The compositional purity of the composites was checked by the Energy Dispersive X-ray Spectra (EDX). The micrographs with EDX

spectra for x = 0.0, x = 1.0 and x = 0.5 are presented in figure 4.4. The EDS spectrum taken at different regions of the samples, confirms the stoichiometry of the samples. The green peaks in the spectra confirm the presence of Bi, Eu, Ni, Zn and Fe in the corresponding composites. The red peaks are mainly for Cu and C and attributed to the sample holder and carbon tape used in the microscopy grid.

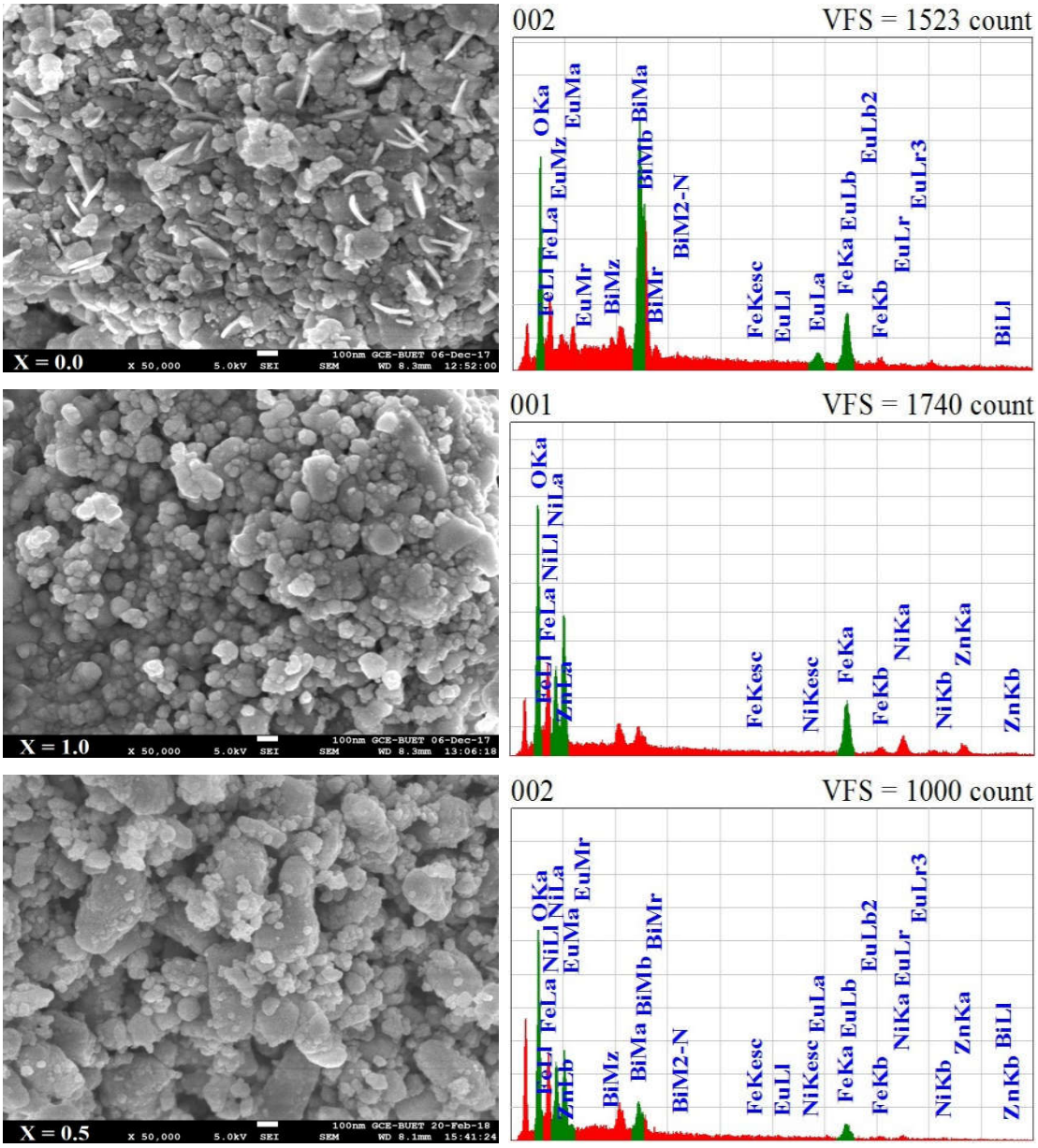

Figure 4.4: FESEM micrographs and EDX spectra of $(1-x)\cdot \mathrm{BEFO} + x\cdot \mathrm{NZF}$ composites x = 0.0, x = 1.0 and x = 0.5

As evident from figure 4.4, the micrographs are comprised of grains closely arranged together with sharp grain boundaries. The grain size was measured by using imageJ software. The scale of FESEM micrographs are 100 nm and the average grain

size is found in (60~70) nm range. So these micrographs are one of the major attestations to admit that the produced samples are in nano scale and the synthesis methodology described in chapter-3 is preferable to produce nano particle.

4.2.1 Study of Microstructure and Morphology with the Variation of Annealing Temperature

It is well known that the properties of the ceramic composites depend strongly on their structure, grain size and density which changes with temperature. The effect of different annealing temperature on particle size and grain growth has been studied by FESEM micrographs at room temperature. Powder BEFO and NZF samples annealed at 300^0 C, 450^0 C, 600^0 C, 750^0 C and 850^0 C were used in FESEM measurement and are shown in figure 4.5. The average grain size of the samples has been determined by the imageJ software and is shown in table 4.2.

Table 4.2: Grain growth of BEFO and NZFO phases with heating temperature

	Average Particle Size (nm)				
Temp.	300^0 C	450^0 C	600^0 C	750^0 C	850^0 C
BEFO	76	72	71	473	821
NZF	67	69	53	81	144

It is seen from the table 4.2 that the grain size of both BEFO and NZFO are comparable in low annealing temperature ranging from 300^0 C to 600^0 C. BEFO grains are found to be slightly larger than NZF grains in this temperature range and are attributed to the larger ionic radius of BEFO than NZF contents and the its relatively low melting temperature. The ionic radius of Bi^{3+}, Eu^{3+}, Ni^{2+}, Zn^{2+} and Fe^{3+} as found in webelements.com are given in table 4.3 which justify that theoretically the grain size of pure BEFO should be greater than that of NZF phase.

Table 4.3: Ionic radius for the elements used in this research

Ion	**Coordination**	**Type**	**Ionic Radius (Å)**
$\mathbf{Bi^{3+}}$	6	octahedral	1.17
$\mathbf{Eu^{3+}}$	6	octahedral	1.03
$\mathbf{Ni^{2+}}$	6	octahedral	0.69
$\mathbf{Zn^{2+}}$	4	tetrahedral	0.74
$\mathbf{Fe^{3+}}$	4	tetrahedral	0.63

At the higher annealing temperature 750^0 C and 850^0 C, the grain size differs largely between BEFO and NZF phases and can be attributed to the difference in melting temperature of the two phases. BEFO phase has melting temperature around 800^0 C and at 750^0 C, it has started to fuse and coagulate. But the NZF phase has the melting temperature above 1200^0 C. So the growth rate of NZF is much slower than the BEFO at the applied annealing temperature. And at the annealing temperature 750^0 C and 850^0 C, it is clearly evident from the FESEM micrographs.

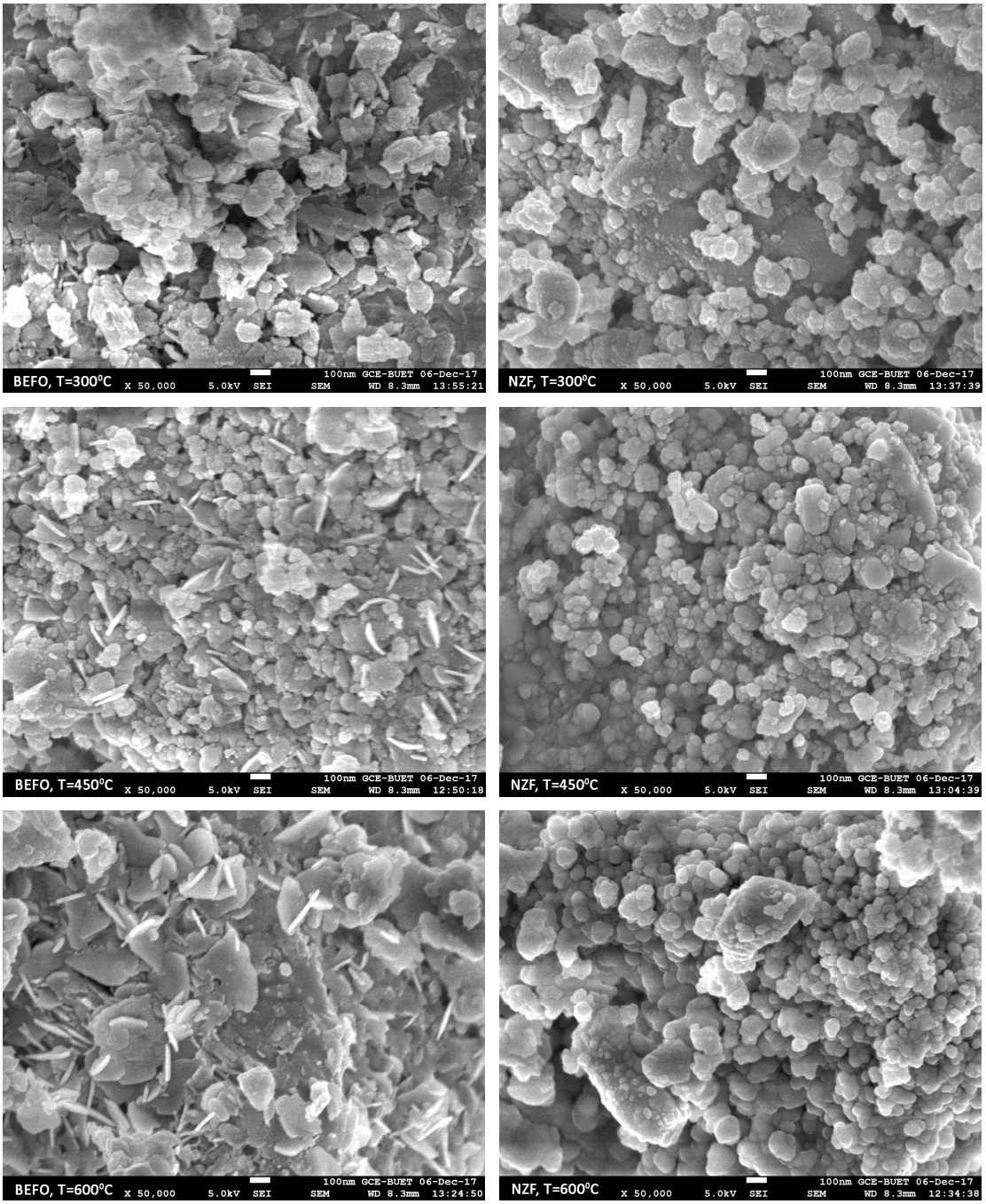

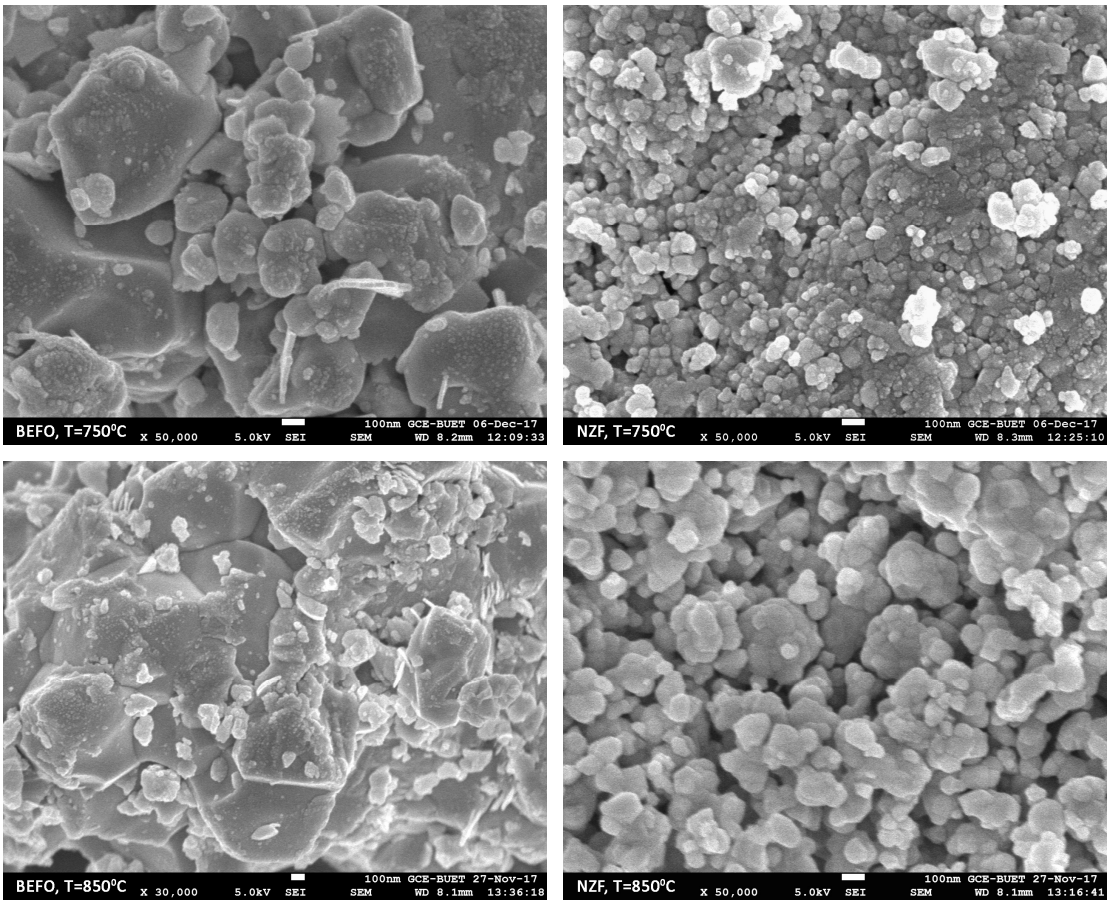

Figure 4.5: FESEM micrographs of BEFO and NZF annealed at 300^0 C, 450^0 C, 600^0 C, 750^0 C and 850^0 C temperature

A grain shape difference is easily seen in the micrographs that the particles of NZF phases are approximately spherical in shape whereas BEFO phases are in lump plate shape form with highly non spherical grains. This indicates that both the BEFO and NZF phase follow their own grain growth style. The NZF nanocrystallites have a tendency to grow in the form of nanospheres via a growth model called oriented aggregation [4.10]. When NZF nanoparticles are not restricted by any functional surfactants, they grow randomly and aggregate in an isotropic way to form smaller spheres. In case of BEFO, Eu leads to a change in morphology from near-spherical shape for pure BFO to highly non-spherical grains tending to form hexagonal shape [4.11]. There are some uneven curved plate-like piece of materials observed in the BEFO phase at annealing temperature 450^0 C and 600^0 C and are known as nanoflake. Nanoflake is a flake with at least one nanometric dimension. In the micrographs, the flakes possess nanometric thickness. Nanoflakes are composed of millions of tiny crystals and adopt an overall structure like them [4.12]. Therefore, the plate shape

nanoflakes of BEFO can be consider as another indication that BEFO has hexagonal structure as confirmed from the XRD spectra.

A comparative grain growth and morphological study of (1-x) [$Bi_{0.9}Eu_{0.1}FeO_3$] + x[$Ni_{0.6}Zn_{0.4}$ Fe_2O_4] (with x = 0.1, 0.3, 0.5 and 0.7) composites annealed at 600^0 C and 850^0 C were done by FESEM and has shown in figure 4.6. In all the micrographs, the samples are found dense and well sintered. The grains of both constituents (BEFO and NZF) in the composites are found closely packed. The strong adhesion between these constituents reveals the successful formation of the proposed composites. An inhomogeneous grain growth has been observed in all the composites which can be attributed to the different growth rate of the individual phases present in the composites. In case of co-fired ceramics, the internal stress cannot be avoided due to the difference in ionic radius, densification rate and thermal expansion coefficient of each phase. This may be the reason for non-uniform microstructure with different grain sizes, which is observed in the composites.

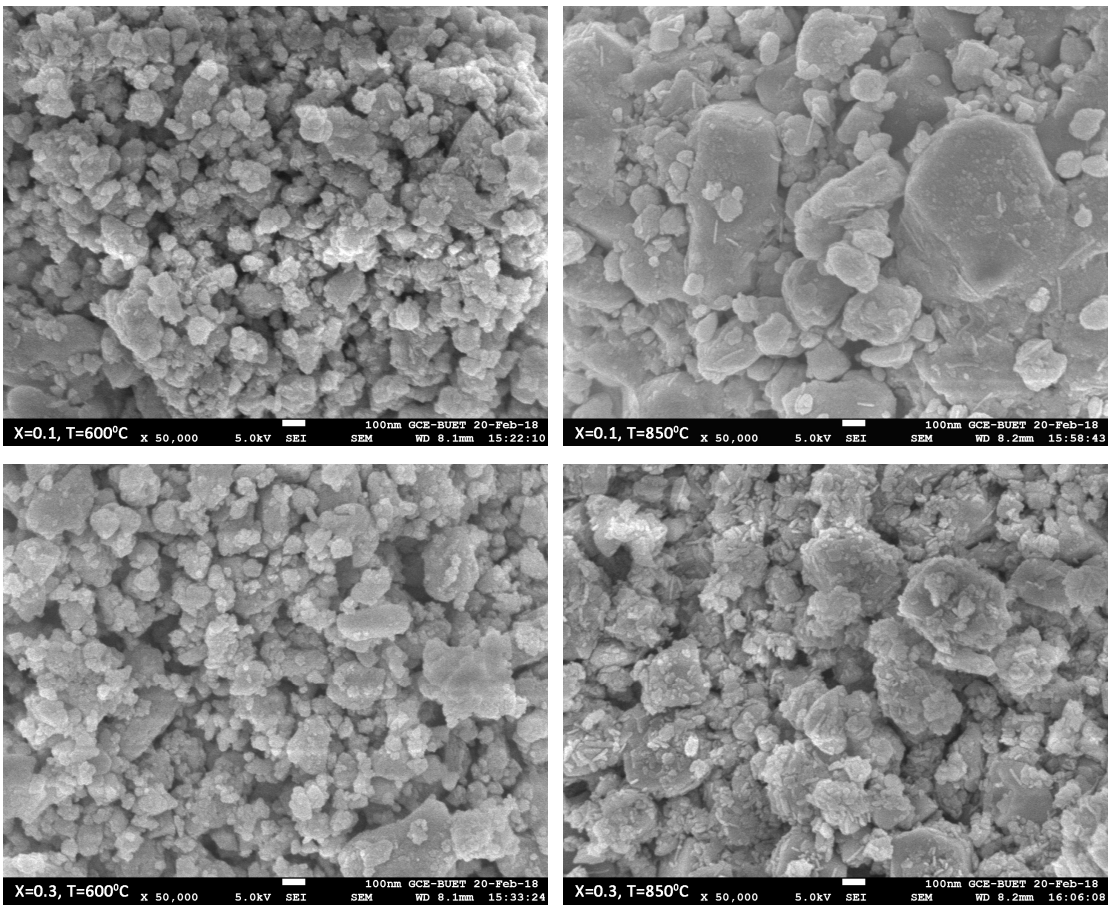

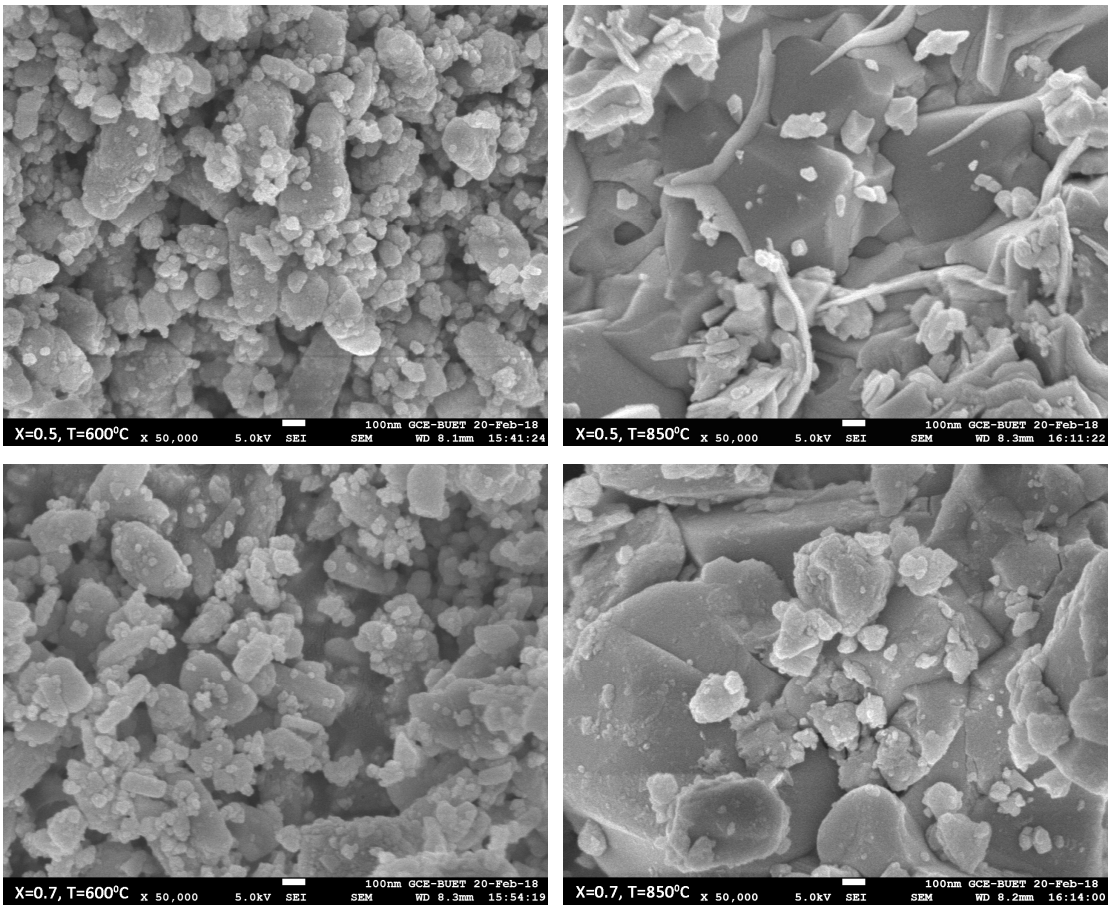

Figure 4.6: FESEM micrographs of $(1-x)\cdot BEFO + x\cdot NZF$ (with x = 0.1, 0.3, 0.5 and 0.7) composites heated at 600^0 C and 850^0 C

The average grain size of the composites was calculated by using imageJ software and has been shown in table-4.4. Due to the highly agglomerate condition, measuring the grain size is a tough job because the grain boundary is not easily visible. Therefore the measurement of grain size may not 100% accurate but only gives an average view. It is found that the grain size has increased with the increasing annealing temperature. The grain growth of composites can be ascribed to the migration of pores in the solid solution to the grain boundary. Moreover, at higher temperature particles with high surface energy tend to stabilize themselves by reducing surface area to volume ratio and therefore increase the grain size.

Again, it is expected that the grain size of the composites will decrease with increasing NZF content. But from the FESEM micrographs of the composites sintered at 850^0 C, it is found that the grain size has decreases for x = 0.1 and then increased for x = 0.5 and x = 0.7. This can be attributed to the secondary phase formed in the BEFO phase as shown in the XRD spectra. The secondary phase has reduced melting

temperature and co-efficient of thermal expansion which affects the overall melting temperature and densification rate of the composite and thus has increased the grain size for x = 0.5 and x = 0.7.

Table 4.4: Grain size of $(1-x)\cdot BEFO + x\cdot NZF$ composites from FESEM micrographs with annealing temperature of 650^0 C and 850^0 C

Annealing Temperature	Contents	Average Grain Size (nm)
600^0C	X = 0.1	88.68
	X = 0.3	86.83
	X = 0.5	118.35
	X = 0.7	121.81
850^0C	X = 0.1	481.57
	X = 0.3	343.98
	X = 0.5	504.81
	X = 0.7	566.21

4.3 Measurement of Ferromagnetic Effect on Multiferroic $(1-x)\cdot BEFO + x\cdot NZF$ Composites

The magnetization curves of the samples were taken by using VSM of Atomic Energy Centre, Dhaka. Small piece of samples of weight (9~11) mg sintered at 850^0 C were taken to obtain the applied magnetic field (H) dependent magnetization (M) curve (M-H curve). To understand the hysteresis behavior full cycle magnetization curves were obtained for an external field up to 10 kOe.

Figure 4.7 shows the M-H curves of $(1-x)\cdot BEFO + x\cdot NZF$ composites with x = 0.0, 0.1, 0.3, 0.5, 0.7 and 1.0. The magnetization increases with increasing applied magnetic field up to a certain value and then becomes saturated with further increase of the applied field. A comparatively larger saturation magnetization (M_S = 10.3128 emu/gm) has observed for BEFO (x = 0.0) phase, though the un-doped BFO posses no net magnetization. It reveals that Eu doping in the Bi-site of BFO has enhanced its magnetic property. The enhancement of magnetization in BEFO is a collective effect of several factors. The ferromagnetic coupling between Eu^{3+} and Fe^{3+} ions is the main reason. In $EuFeO_3$ orthoferrite, $Fe^{3+}\leftrightarrow Fe^{3+}$, $Eu^{3+}\leftrightarrow Fe^{3+}$ and $Eu^{3+}\leftrightarrow Eu^{3+}$ exchange interactions coexist due to the presence of two magnetic sublattices of Fe^{3+} and Eu^{3+}. In pure BFO phase the $Fe^{3+}\leftrightarrow O\leftrightarrow Fe^{3+}$ super-exchange interaction dominates, giving rise to AFM ordering. With Eu doping in BFO lattice, the interactions between the

$Eu^{3+}\leftrightarrow Eu^{3+}$ and $Eu^{3+}\leftrightarrow Fe^{3+}$ ions decouple the anti-ferromagnetic interactions between the Fe^{3+} ions and contribute to Weak Ferromagnetic ordering [4.3].

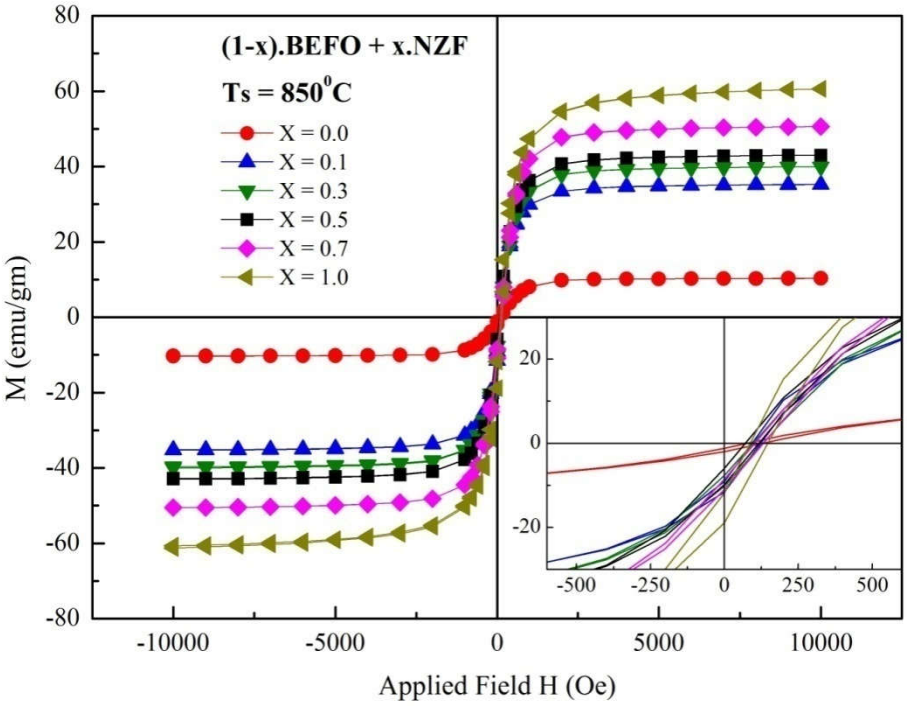

Figure 4.7: Magnetization M-H curve of $(1-x)\cdot BEFO + x\cdot NZF$ composites sintered at 850^0 C temperature

The Eu^{3+} ion has smaller ion radius (1.07 Å) that Bi^{3+} (1.17 Å) and substitutes it in perovskite type unit cell. Eu doping in BFO decreases the crystallite size and Fe-O-Fe bond length and consequently increases the micro strain in the lattice. This can lead to larger distortion and also contribute partly to the enhanced magnetization. Moreover, the anti symmetric Dzyaloshinskii–Moriya (DM) exchange interaction between neighboring spins induced by the spin–orbit interaction also contributes to the WFM observed in the figure 4.7 [4.13].

The large value of saturation magnetization found at x=1.0 can be described by the cation distribution in A and B-sites of NZF. This can be understood in terms of the A↔B, A↔A and B↔B interactions where the effect of A↔B interaction is by far the greatest. In un-doped $NiFe_2O_4$ structure Fe^{3+} ions occupy the tetrahedral A-sites and $Ni^{2+}\leftrightarrow Fe^{3+}$ ions occupy the octahedral B-sites. When non-magnetic zinc ions are substituted for Nickel and as it prefers to go to A-sites, the Fe^{3+} ions are pushed from A to B sites. In other words, the non-magnetic ion at A-site increases that means the magnetization at the A-site decreases while at the B-site increases. Because of the relative magnitudes of the exchange interactions, the spins of the A and B site ions in

ferrites with spinel structure are expected to be oppositely oriented. So at temperature T, there will be two saturated and oppositely magnetized sublattices present. The resultant magnetization is thus the difference between the magnetization of the octahedral lattice (B) and that of the tetrahedral lattice (A).

$$M = M_B - M_A \quad (4.1)$$

Where M_A and M_B are the magnetic moment of A and B sites respectively.

As the substitution of Zn content (on the A-site) leads to decrease the magnetization of A-site and increase the magnetization of B-site, it is therefore increases the net magnetization of NZF [4.14]. Magnetic parameters such as saturation magnetization (M_S), coercive field (H_C), remanent magnetization (M_r), magnetic moment in Bohr magneton (μ_B) and the approximate anisotropy constant (k_1) are measured from the magnetic hysteresis loop and are presented in table 4.5.

Table 4.5: Magnetic parameters M_S, H_C, M_r, μ_B and k_1 of $(1-x)\cdot BEFO + x\cdot NZF$ composites for different x sintered at 850^0 C

Composition (x)	M_S (emu/gm)	H_C (Oe)	M_r (emu/gm)	Magnetic moment (μ_B)	Anisotropy constant ($\geq k_1$)
0.0	10.31	24.59	0.38	0.57	126.80
0.1	35.24	14.02	1.24	1.90	247.07
0.3	39.93	16.31	1.28	2.06	325.71
0.5	42.98	23.03	1.95	2.11	495.01
0.7	50.54	14.44	1.21	2.37	364.75
1.0	60.94	29.59	3.54	2.64	901.44

It is seen that the saturation magnetization M_S of the composite increases with the increase of NZF component and closely follows the rule of mixtures expressed as

$$M(x, H) = x\cdot M(1.0, H) + (1-x)\cdot M(0.0, H) \quad (4.2)$$

Where M(x, H) is the magnetization for composite with x weight fraction and H is the applied field strength.

However, the magnetic parameters M_r and H_C do not follow the rule of mixture as shown in the table 4.5. It indicates the existence of inter-grain exchange coupling between the two different phases of the composites [4.15]. The incorporation of NZF on BEFO leads to enhancement of magnetization as the interfacial strain present in the composites leads to change the orientation of the spin [4.16]. The composites exhibit a low value of coercivity than the pure BEFO which means that with addition of NZF content magnetization can be realized more easily.

The calculation of magnetic moment in Bohr magneton was carried out using the following relation.

$$\mu_B = \frac{M \cdot \sigma_s}{5584.8028} \tag{4.3}$$

Where M is molecular weight, σ_s is the magnetization per gram mol of the sample and 5584.8028 is the magnetic factor. The values of saturation magnetization Ms and Bohr magneton (μ_B) are found to increase with an increase of NZF content. This is attributed to the spontaneous magnetization existing in the composites. The spontaneous magnetization of the composites is originated from the unbalanced anti-parallel spins which lead to the net spins [4.17]. Moreover it has been predicted that in the in the composites containing ferrite and ferroelectric phases, each ferrite grain is in contact with the ferroelectric grain and this connection is increased with addition of ferrite content and hence Ms and μ_B.

In the inset of figure 4.7, it is seen that the hysteresis curves of the samples have been shifted to the right from the origin and is attributed to the exchange bias effect. Exchange bias occurs in interfaces of anti-ferromagnetic and ferromagnetic materials, where the hard magnetization behavior of an anti-ferromagnetic material causes a shift in the soft magnetization curve of a ferromagnetic material [4.18].

In the prepared $(1-x)\cdot BEFO + x\cdot NZF$ composites BEFO shows very weak ferromagnetic behavior whereas NZF is strong ferromagnetic. The soft ferromagnetic NZF is strongly coupled with the weak ferromagnetic BEFO in the composites and has its interfacial spins pinned. Therefore at the time of magnetization, reversal of the NZF moment will require an additional energy to create a Néel domain wall in the BEFO interfaces. The added energy term implies a shift in the switching field of the NZF. Thus the magnetization curve of the composites shifts from the origin.

4.4 Study of the Frequency Dependent Complex Permeability

Permeability is one of the most important parameters in evaluating the magnetic properties of a material. It is a measure of the ease in magnetization of a material. The magnetic permeability under an oscillatory electromagnetic field is a complex quantity and can be expressed as

$$\mu^* = \mu' - i\mu'' \tag{4.4}$$

Where μ' and μ" are the real and imaginary part of the complex initial permeability respectively.

To know about the magnetic behavior of the samples, frequency dependent permeability was measured over a wide range of frequency from 1 KHz to 100 MHz. Figure 4.8 represents the frequency dependent μ' for BEFO and NZF along with their composites. It is seen that μ' remains almost constant until very high frequency (around $5x10^7$ Hz) and then drops rapidly. The fairly constant μ' values over a wide range of frequency region are known as the zone of utility because it demonstrates the compositional stability and quality of the prepared samples. This characteristic is anticipated for various applications such as broadband pulse transformer and wide band read-write heads for video recording [4.19].

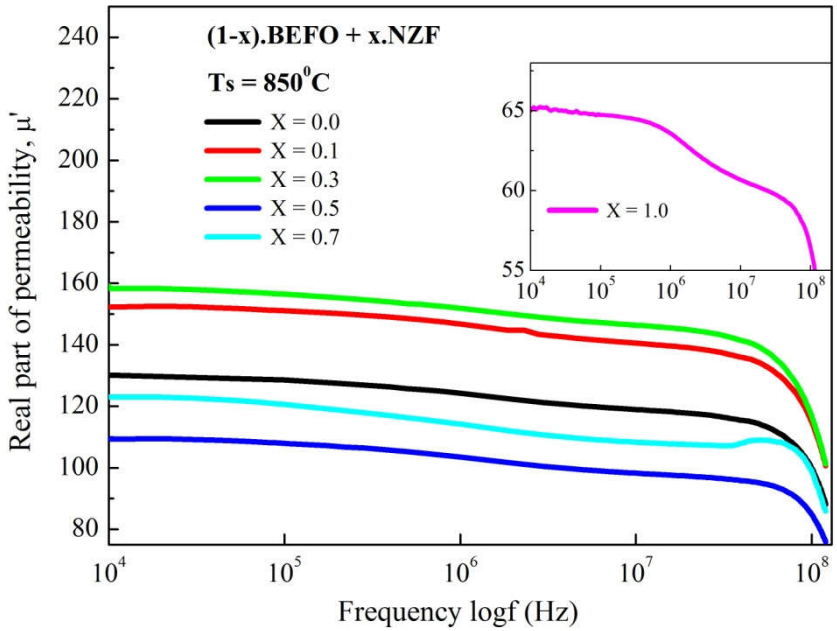

Figure 4.8: Frequency dependent real part of permeability of $(1-x)\cdot BEFO + x\cdot NZF$ composites with x = 0.0, 0.1, 0.3, 0.5, 0.7 and 1.0 sintered at 850^0 C

In the prepared composite, the BEFO component is actually a weak ferro-magnetic, while NZF component is a soft magnetic material. So it was expected that the magnetic permeability of the composites should increase with the increase of NZF content. But from the figure 4.8 it is observed that μ' has first increased for x = 0.1 and x = 0.3 and then decreased with increasing NZF content. It can be explained with the effect of grain size and porosity on μ'. Generally, a pore in a magnetic material affects the permeability via the decrease in magnetization per unit volume and via the increase in the demagnetizing field. The calculated porosity of the samples have shown in table 4.1 and for NZF content it is 49.37%, which is much higher than any other of the prepared samples. So there should be a decrease in permeability.

Another thing that can affect the permeability is the grain size. Generally, the grain boundary disturbs the magnetic wall movement and also the magnetic dipoles appear on the grain boundary surfaces. Globus et al. [4.20] have derived a relation between the permeability and the grain size and showed that

$$(\mu - 1) \propto r \qquad (4.5)$$

Where, r is the radius of the sphere of crystallite grain.

From Eq^{n}. (4.5), the permeability of a sample is proportional to its grain size. From the FESEM micrographs the average grain size of NZF phase sintered at 850^0 C is found 144.303 nm, quiet lower than any of the other prepared samples. So this is another reason to find lower μ' of NZF in this study. The most enhanced permeability is observed for x = 0.1 and can be attributed to have the least porosity (16.297%) and enlarged particle size (481.571 nm).

All ferrite materials reveal a ferromagnetic (or spin) resonance frequency at which the permeability drops to a low value and a peak is generated which refers magnetic losses. Snoke's low is a good argument to describe this phenomenon. According to Snoke's relation ($f_r\mu' = \text{constant}$) [4.21] high cut-off frequency (f_r) and high permeability are mutually incompatible. That means, material with higher value of permeability has lower cut-off frequency. From the figure 4.8, it is observed that the prepared samples have followed the Snoek's relation.

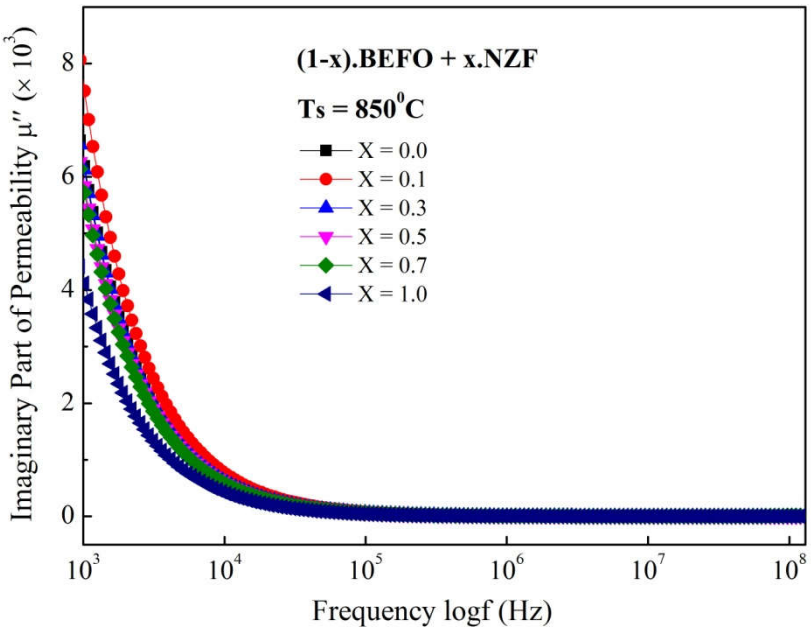

Figure 4.9: Frequency dependent Imaginary Part of Permeability of $(1 - x) \cdot \text{BEFO} + x \cdot \text{NZF}$ composites with x = 0.0, 0.1, 0.3, 0.5, 0.7 and 1 sintered at 850^0 C

Figure 4.9 shows the variation of imaginary part of permeability μ" with frequency. It describes the losses of energy by the oscillatory field in such magnetic medium. From the figure 4.9 it is observed that μ" has decreased for all the samples at lower frequency and then comes to an outstanding stability at the higher frequency region which is a good deal for industrial application.

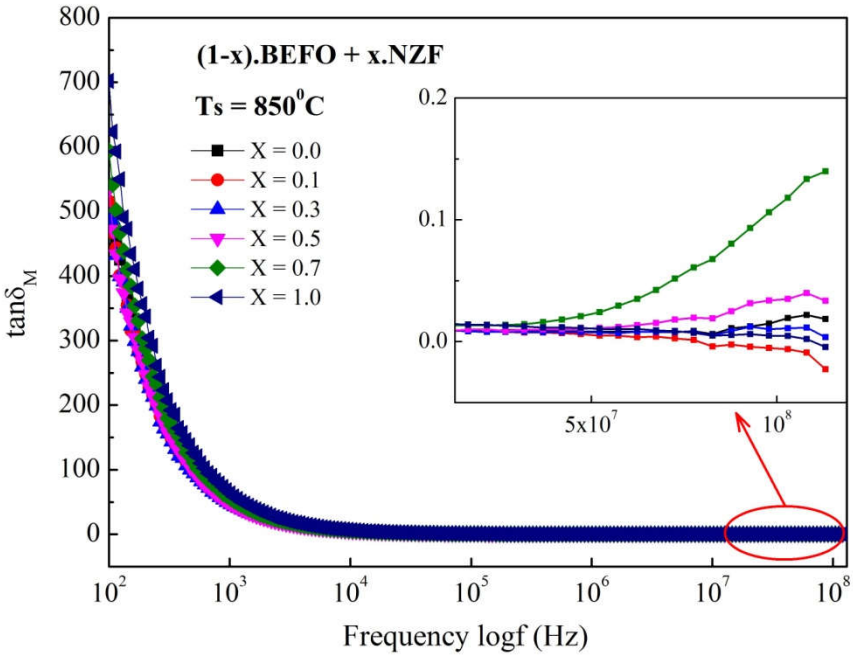

Figure 4.10: Frequency dependent loss tangent of $(1-x)\cdot BEFO + x\cdot NZF$ composites with x = 0.0, 0.1, 0.3, 0.5, 0.7 and 1 sintered at 850^0 C

Figure 4.10 shows the loss tangent $(\tan\delta_M = \frac{\mu''}{\mu'})$ of the composites as a function of frequency. This is a measure of the inefficiency of the magnetic system and is highly desirable to have this as low as possible from the application point of view. At the lower frequency region, the magnetic loss tangent decreases rapidly with the increase of frequency. After 10 KHz it becomes constant and doesn't change over a large frequency range. The $\tan\delta_M$ is sensitive to many factors such as humidity, porosity, concentration of dipoles, mobility of charge carriers, domain defects, eddy current loss hysteresis loss and residual loss [4.22].

In this study, $\tan\delta_M$ increases with the increase of NZF content, which can be attributed to the high porosity of NZF phase. At high frequency $(f > 5\times10^7$ Hz), $\tan\delta_M$ increases as shown in the inset of figure 4.10, which is due to the increased eddy current loss. At low or medium frequencies the reduction of the magnetizing field through eddy current is low as the size is not very large. There is a time factor

involved in the depth of penetration. At low frequencies there is sufficient time for the eddy currents to dissipate. At higher frequency, there is insufficient time for eddy currents to decay and so the reverse fields will become appreciable. These increased eddy currents shield the inside of the sample from the applied field and therefore increased the loss tangent [4.22].

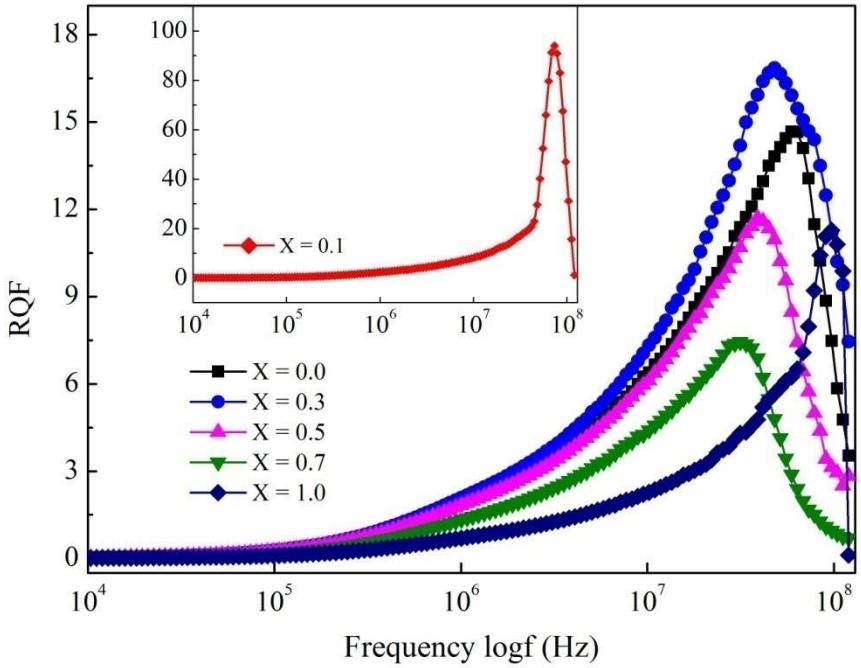

Figure 4.11: Frequency dependent relative quality factor of $(1-x)\cdot \mathrm{BEFO} + x\cdot \mathrm{NZF}$ composites with x = 0.0, 0.1, 0.3, 0.5, 0.7 and 1.0 sintered at 850^0 C

Figure 4.11 represents the relative quality factor (RQF) of the prepared sample as a function of frequency. It is a measure to show the performance of the sample. Higher RQF indicates a lower rate of energy loss relative to the stored energy. The highest value of RQF is observed for 0.9 BEFO + 0.1 NZF composite, which has lowest tan δ_M and also the lowest porosity (16.297%).

4.5 Study of the Frequency Dependent Dielectric Properties

Figure 4.12 shows the variation of dielectric constant (ε') as a function of frequency up to 1 MHz for the $(1-x)\cdot \mathrm{BEFO} + x\cdot \mathrm{NZF}$ composites along with the dielectric responses of single phase BEFO and NZF. It is observed that the value of ε' decreases with the increase in frequency up to100 kHz, after that it remains almost constant for all the samples. This is due to the inability of electric dipoles to follow up the rapid variation of the alternating applied electric field. These frequency independent values are known as static values of the dielectric constant.

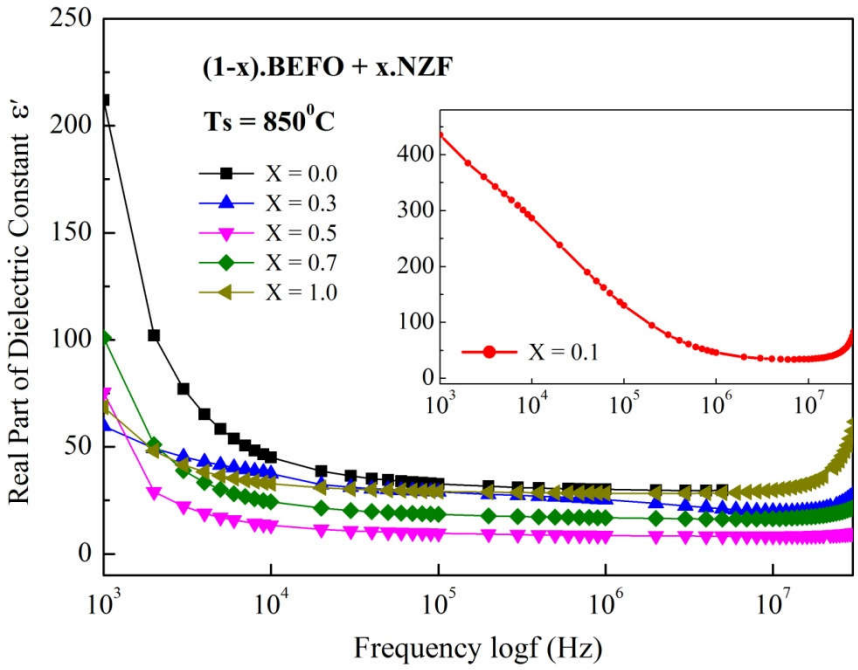

Figure 4.12: Frequency dependent real part of dielectric constant of $(1-x)\cdot BEFO + x\cdot NZF$ composites with x = 0.0, 0.1, 0.3, 0.5, 0.7 and 1.0 sintered at 850^0 C

The dielectric dispersion at lower frequency can be described with the help of four fundamental polarization mechanisms exist in the composites [4.23]. They are electronic, ionic, dipolar or orientational and space-charge or interfacial polarization. On application of electric field, the displacement of electron cloud relative to nuclei in the atom leads to electronic polarization while the increased inter ionic separation between the positive and negative ions results in ionic polarization. Similarly, the tendency of orientation of dipoles along the field direction gives rise to dipolar polarization whereas the accumulation of charges at the inter-phase interface in a composite gives rise to the interfacial polarization. At lower frequencies all four types of polarizations are present but at higher frequency the dielectric dispersion are made mostly from the dipolar and interfacial mechanisms only.

This can be described by the Koop's phenomenological theory based on the Maxwell-Wagner model considering inhomogeneous double layer dielectric structure. The Koop's theory assumes that the composites are composed of well conducting grains separated by poorly conducting grain boundaries. The poorly conducting grain boundaries have been found to be effective at lower frequencies while the fairly conducting grains are effective at higher frequencies. Therefore, ε' are found higher at lower frequencies and decreases with the increasing frequency [4.6].

Now, before evaluating the dielectric behavior of the $(1-x)\cdot BEFO + x\cdot NZF$ composite, let us first have a close look at the dielectric response of the single phase BEFO and NZF samples as they form the integral parts of the composite structure. The undoped BFO is found to be very low in dielectric dispersion, but the dielectric constant increases dramatically with Eu doping on the Bi-site [4.24]. This dielectric behavior of Eu doped BFO ceramics might be understood in terms of oxygen vacancy and the displacement of Fe^{3+} ions. Due to the volatilization of Bi in sintering process, there are always some oxygen vacancies in pure BFO, which results in relatively high conductivity and small dielectric constant (ε′). The substitution of Eu^{3+} for Bi^{3+} in a certain range would stabilize the perovskite structure of BFO, and hence reduces the density of oxygen vacancies and subsequently increases the dielectric constant.

Dielectric polarization in NZF has largely been attributed to the presence of Fe^{2+} ions which gives rise to heterogeneous spinel structure. Since Fe^{2+} ions are easily polarizable, the larger the value of Fe^{2+} ions, the higher would be the dielectric constant. In NZF ferrite system, two probable conduction mechanisms, via electron hopping between Fe^{3+} and Fe^{2+} and hole hopping between Ni^{3+} and Ni^{2+} must be operative. Moreover, the presence of Ni^{2+}/Ni^{3+} and Zn^{2+}/Zn^{3+} ions give rise to p-type carriers, which also contributes to the polarization mechanism in addition to n-type carriers i.e., electronic exchange between $Fe^{2+}\leftrightarrow Fe^{3+}$ ions. The contribution of p-type carriers should be smaller than n-type carriers so even at lower frequencies their contribution to polarization decreases more rapidly. Hence, initially the polarization increases and afterwards it decreases with increasing frequency [4.25].

As dielectric property is sum property, so according to simple rule of mixture, the dielectric properties of two phase composites are approximately given by [4.26].

$$\varepsilon_{eff} = (1-\varphi)\cdot\varepsilon_1 + \varphi\cdot\varepsilon_2 \qquad (4.6)$$

Where ε_{eff} is the effective dielectric constant of composite, and ε_1 and ε_2 are dielectric constants corresponding to BEFO and NZF phases respectively and $(1-\varphi)$ is the volume fraction of NZF phase.

From figure 4.12 it is observed that the obtained values do not follow the rule of mixture indicating the interface interaction between the BEFO and NZF grains in the composites which lead to the random behavior of dielectric constant [4.27]. At lower frequency region, the dielectric constant has increased with the addition of NZF content with BEFO and becomes maximum for x = 0.1. This can be attributed to the

least porosity 16.3%, increased bulk density 6.7gm/cm^3 and high grain size 481.57nm. The increase of average grain size leads to reduction of grain boundary area which acts as an obstacle for domain wall motion. The mean free path of electrons increases and hence the dielectric constant [4.28, 4.29]. A relatively low dielectric constant has been observed in NZF phase and attributed to the largest porosity (49.37%) of the NZF phase. In porous material, the interfacial polarization among the grains get reduced which reduces the dielectric constant.

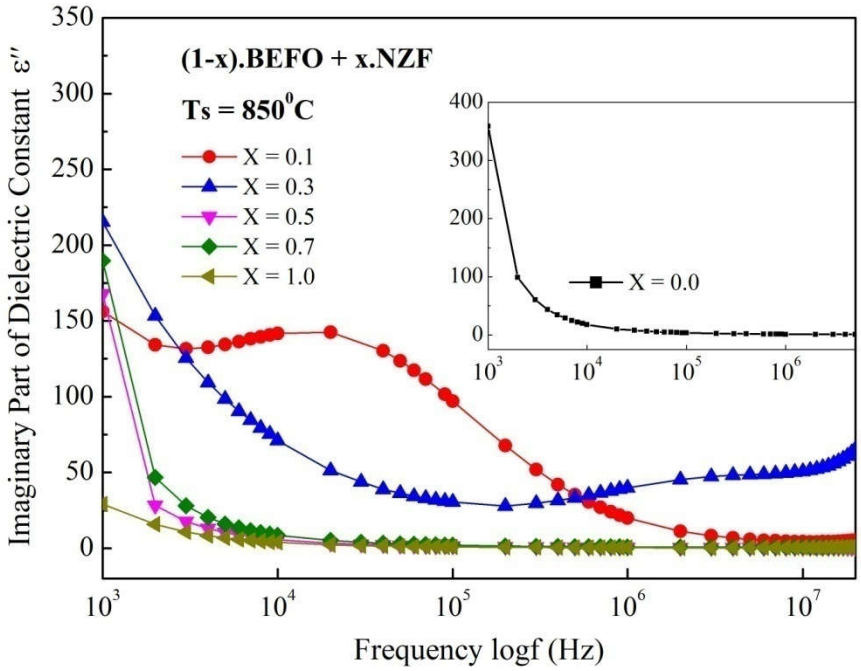

Figure 4.13: Frequency dependent imaginary part of dielectric constant of $(1-x)\cdot BEFO + x\cdot NZF$ composites with x = 0.0, 0.1, 0.3, 0.5, 0.7 and 1.0 sintered at 850^0 C

Figure 4.13 represents the imaginary part of dielectric constant (ε") of $(1-x)\cdot BEFO + x\cdot NZF$ composites with x values of 0.0, 0.1, 0.3, 0.5, 0.7 and 1.0. It is a measure of energy absorption in a system as a result of neutral charge excitation. It is also a measure of energy loss. It represents conversion from electromagnetic to thermal energy. From figure 4.13 it is observed that ε" is maximum for x = 0.0 and minimum for x = 1.0 and linearly decreased with increasing ferrite content. An increasing peak is observed for x = 0.1 at 10^4 to 10^5 Hz which can be attributed to the distortion in space charge distribution. The decrease in ε" with increasing frequency agrees with Debye's type relaxation process [4.31- 4.32].

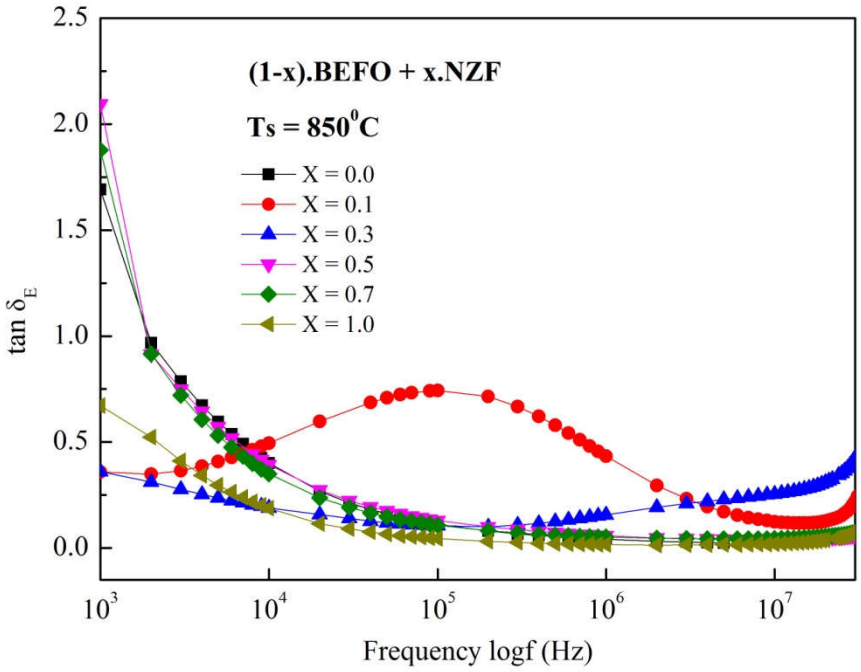

Figure 4.14: Frequency dependent dielectric loss tangent of $(1-x)\cdot BEFO + x\cdot NZF$ composites with x = 0.0, 0.1, 0.3, 0.5, 0.7 and 1.0 sintered at 850^0 C

Figure 4.14 shows the variation of dielectric loss tangent (tan δ_E) of single phase BEFO and NZF along with their corresponding BEFO–NZF composites at room temperature as a function of frequency up to 1MHz. As expected in ferrites and multiferroics [4.33] the tan δ_E decreases with the increase in frequency, and the rate of decreasing is higher at lower frequencies whereas it remains almost independent with frequency at higher frequencies.

The observed dielectric loss tangent behavior in the present study can be explained as follows: The tan δ_E depends on several factors, such as stoichiometry, Fe^{2+} and Eu^{3+} concentrations, and structural homogeneity, which in turn depend on the sintering temperature and composition of the samples [4.34, 4.35]. Further, the microstructures of the composites are composed of grains, grain boundaries and structural defects such as pores, impurities etc. Moreover, the samples in general exhibit high resistivity's at low frequencies due to contributions of resistance by grain boundaries. The high resistance offered by the material makes the electron flow difficult within the material and thus relatively large amount of energy is needed for electronic exchange between $Fe^{2+}\leftrightarrow Fe^{3+}$ and $Eu^{3+}\leftrightarrow Eu^{4+}$ ions which results in larger dielectric loss at low frequencies in these materials. Whereas in the high frequency region, which corresponds to a low resistivity region, small energy is required for electron transfer between the crystallographically equivalent but different valence

ions of Fe and Eu at the same lattice sites and so the low dielectric loss is observed. The dielectric loss of the composites is less than that of the ferroelectric BEFO phase both in the low and high frequency regions. Therefore, the composites could potentially be utilized as a part of handy applications, for example, magnetically tunable filters, resonators and oscillators.

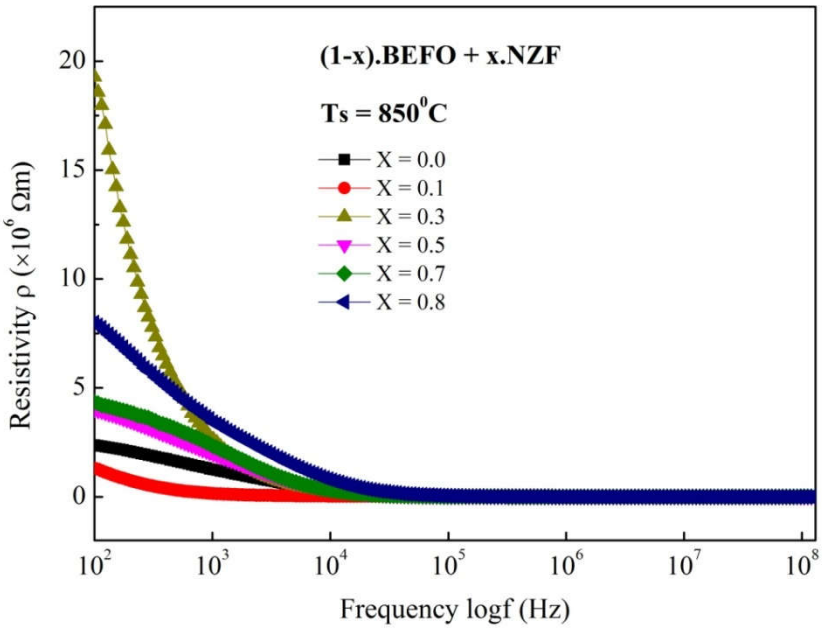

Figure 4.15: Frequency dependent resistivity of $(1-x)\cdot BEFO + x\cdot NZF$ composites with x = 0.0, 0.1, 0.3, 0.5, 0.7 and 1.0 sintered at 850^0 C

Figure 4.15 represents the frequency dependent resistivity of the $(1-x)\cdot BEFO + x\cdot NZF$ composites with different x values of 0.0, 0.1, 0.3, 0.5, 0.7 and 1.0. The resistivity has been found to decrease with the increase in the frequency (f) of the applied a.c current. The dependence of resistivity on frequency (f) can be interpreted in terms of inter-granular gap resistance. In the composites, particles are separated from each other by inter-granular grain boundaries. Though the particles are fairly conductor of current but the grain boundaries are bad conductor. Therefore at low frequency electrons face obstacle from the grain boundaries resistance. At the larger frequency, the inter-granular gap resistance becomes short circuited by the inter-granular capacitance and the capacitive shortcuts provide paths to connect the grains electrically and as a result the resistivity decreases [4.36]. It is seen from the figure 4.15 that the resistivity is maximum for x = 1.0 which is fully ferromagnetic NZF content. A comparatively lower resistivity has been observed for x = 0.0 and can be attributed to the ferroelectric nature of the BEFO content but the lowest resistivity has

been observed for x = 0.1 composite. This can be attributed to the maximum density (6.7 gm/cm^{-3}) and minimum porosity (16.29 %) of the composite. In x = 0.1 the inter-granular gap in minimum, so the grains can easily be short circuited and increase the electric conductivity which in turn decreases the resistivity.

4.6 Finding the Optimum Value

The motivation of this thesis was to obtain optimum compositions where both of ferroelectric and ferromagnetic orders contribute to the successful development of multiferroic material. In this study, though the BEFO phase is multiferroic in nature, it possesses strong ferroelectric properties but weak ferromagnetic properties as discussed in the previous section. The NZF phase is a well established ferromagnetic element. But it is not possible to provide strong multiferroic parameters by a single ferroic ordered material. Even their composites may also not have the optimum multiferroic properties and magnetoelectric coupling in all mass fractions. To obtain the optimum mass fraction of the composites, I have cross checked the magnetic and electric properties of the composites. Table 4.6, demonstrates the different values of permeability, magnetic loss tangent, dielectric constant, and dielectric loss tangent of (1-x) [$Bi_{0.9}Eu_{0.1}FeO_3$] + x [$Ni_{0.6}Zn_{0.4}Fe_2O_4$] composites with x values of 0.0, 0.1, 0.3, 0.5, 0.7 and 1.0 sintered at 850^0 C at 1KHz frequency.

Table 4.6: The comparison between permeability, magnetic loss tangent, dielectric constant, dielectric loss tangent of $(1-x)\cdot \mathrm{BEFO} + x\cdot \mathrm{NZF}$ composites with x = 0, 0.1, 0.3, 0.5, 0.7 and 1.0 sintered at 850^0 C

Content (x)	Magnetic Permeability	Magnetic Loss Tangent	Dielectric Constant	Dielectric Loss Tangent
0.0	133.726	49.965	212	1.69
0.1	155.425	47.391	435.03	0.359
0.3	162.422	46.334	59.66	0.361
0.5	111.373	47.243	75.51	2.09
0.7	126.634	55.378	101.08	1.8
1.0	65.279	63.034	68.63	0.672

Figure 4.16 represents the variation of Dielectric constant and magnetic permeability of $(1-x)\cdot \mathrm{BEFO} + x\cdot \mathrm{NZF}$ composites along with their contents. It is observed from the figure that for x = 0.1 to 0.2 both the permeability and dielectric constant has become optimized.

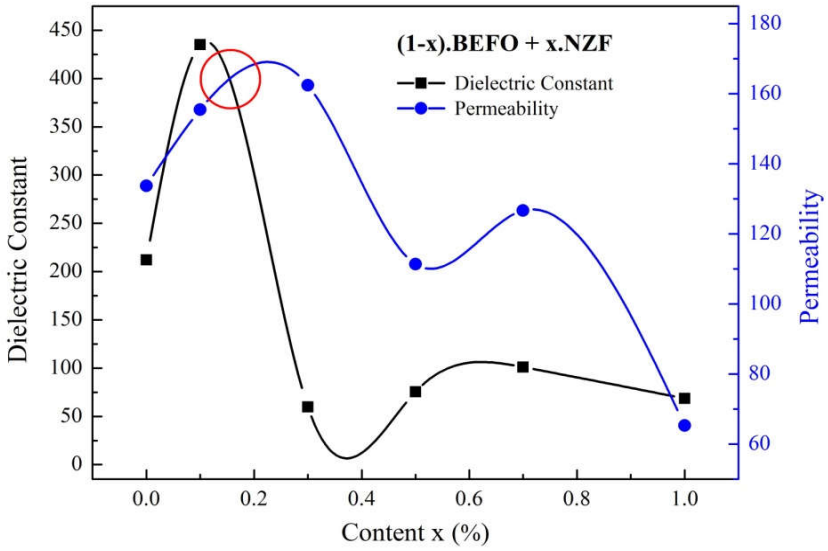

Figure 4.16: Comparison between Dielectric constant and Magnetic permeability of $(1-x)\cdot \mathrm{BEFO} + x\cdot \mathrm{NZF}$ composites with x = 0.0, 0.1, 0.3, 0.5, 0.7 and 1.0 sintered at 850^0 C

From figure 4.17 it is observed that both the dielectric and magnetic loss tangent have become minimum for the mass fraction of x = 0.1. Moreover from figure 4.15, the composite for x = 0.1 shows the minimum resistivity. Therefore, based on the above discussion, for mass fraction x = 0.1 the composite shows the most magneto electric coupling and multiferroic properties.

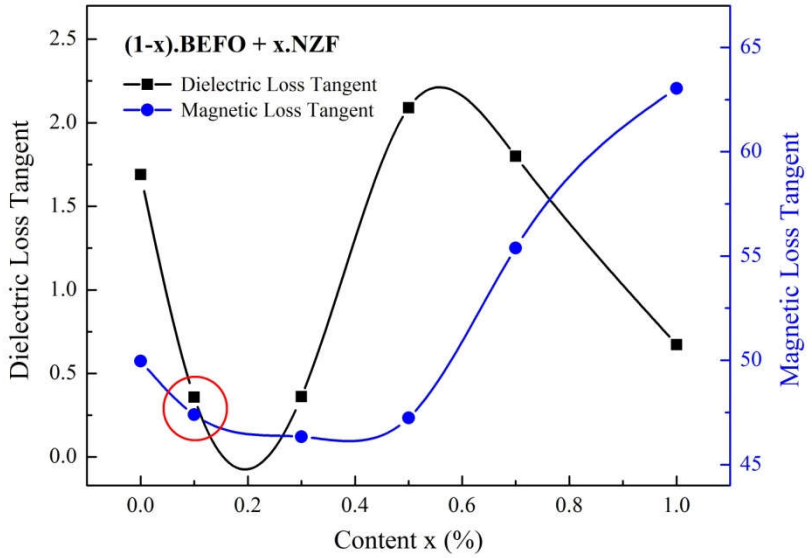

Figure 4.17: Comparison between Dielectric and Magnetic loss tangent of $(1-x)\cdot \mathrm{BEFO} + x\cdot \mathrm{NZF}$ composites with x = 0.0, 0.1, 0.3, 0.5, 0.7 and 1.0 sintered at 850^0 C

CHAPTER V

CONCLUSIONS

CONCLUSIONS

5.1 Conclusions

Multiferroic Composites with different mass ratios of Europium doped Bismuth Ferrite (BEFO) and Nickel Zinc Ferrite (NZF) with general formula (1-x)[$Bi_{0.9}Eu_{0.1}FeO_3$] + x[$Ni_{0.6}Zn_{0.4}Fe_2O_4$] for x=0.0, 0.1, 0.3, 0.5, 0.7 and 1.0 were successfully prepared by the conventional solid state reaction method with different dispersion techniques aided by stirring, power ultrasonification and centrifugation. The powder samples were annealed at 300^o C, 450^o C, 600^o C, 750^o C and 850^o C and pallet and toroid shaped samples were sintered at 850^o C. Powdered samples were used in XRD and FESEM experiments, pallets were used for dielectric measurement and toroids were used for the permeability and magnetization measurements.

From the systematic investigation on the crystallization, structural and magnetic properties the following conclusions:

(i) The XRD patterns of the prepared samples confirm the successful phase formation of rhombohedrally distorted perovskite BEFO phase and cubic spinel NZF phase. The XRD analysis of the composite reveals the coexistence of both the ferroelectric BEFO and ferrite NZF phase in the composite with no chemical reaction.

(ii) The FESEM micrographs have confirmed the successful preparation of nano grains. The average grain size has been found in between (65 - 80) nm over a wide range of temperature (300^o C – 600^o C). The micrographs reveal that the BEFO and NZF phases show different trend of grain growth. The NZF phase follows the growth model called oriented aggregation and has formed spherical nano particles. But in case of BEFO, Eu has lead to a change in morphology from near-spherical shape of pure BFO to highly non-spherical grains with the hexagonal shape.

(iii) The compositional purity of the prepared samples was checked by the EDS spectra and it confirms the presence of the pronounced elements on the composites.

(iv) To understand the effect of annealing temperature on grain growth, The single phase BEFO and NZF were heated at different temperature and found the

grain size larger for BEFO that NZF phase at every temperature. The effect of annealing temperature on composites were also studied and found decreasing with increasing NZF content.

(v) The magnetization measurement of the prepared samples was carried out by VSM. An enhanced magnetization is observed in BEFO than the pure BFO and can be attributed to the magnetically active Eu dopant. The saturation magnetization is found increasing with increasing NZF content. But the remanant magnetization and coercivity do not follow the same trend indicating the inter-grain exchange coupling between the BEFO and NZF phases in the composites. Shift of hysteresis curves from the origin is observed and attributed to the exchange bias effect between the antiferromagnetic BEFO phase and strong ferromagnetic NZF phase.

(vi) The frequency dependent complex initial permeability was measured for the prepared samples. The μ' is first increased with NZF content till $x = 0.3$ and then decreased with NZF content. It can be attributed to the increased ρ_b and reduced porosity of $x = 0.1$ and $x = 0.3$ composite, where the NZF content is considered to fill the pore of BEFO due to its smaller ionic radius. Effect of eddy current has been observed in tan δ_M at higher frequency range. The composites for $y = 0.1$ shows the highest RQF

(vii) The dielectric dispersion at lower frequencies is observed due to interfacial polarization. The ε' shows excellent frequency stability in the high frequency region due to the inability of the electric dipoles to follow up the rapid variation of alternating applied electric field. The dielectric loss decreases at higher frequencies due to the suppression of domain wall motion

(viii) The maximum dielectric constant and magnetic permeability has been observed around $x = 0.1$. Similarly both the magnetic and dielectric loss is found minimum for $x = 0.1$. So from this result it can easily concluded that the optimum multiferroic parameters can get from the composition of $x = 0.1$.

5.2 Scope for Future Work

Further studies can be possible on different features for inherent interest of the present studied materials.

(i) The characteristics in crystallization formation will be achieved by DSC thermal analysis.

(ii) Polarization versus electric field P-E loop measurement can be executed to know the ferroelectric behavior of the studied composites.

(iii) Magnetoelectric coefficient can be measured to understand its degree of multiferroic behavior.

(iv) Neutron diffraction analysis can be performed for the present compositions to obtain the distribution of the substituted ions between the A- and B- sites.

(v) Mössbaurer Spectroscopy can be carried out to know the cation distribution in the A- and the B- sites and to have information about the valance state of the ions.

(vi) Temperature dependent magnetization and dielectric properties will be carried out to understand the effect of temperature on multiferoic parameters.

(vii) To observe the nano size, TEM analysis is required.

REFERENCES

REFERENCES

CHPATER-I

[1.1] "Craniology and the Adoption of the Three-Age System in Britain", Cambridge Press, Retrieved December 27, 2016.

[1.2] Schmid H.; "Multi-ferroic magnetoelectrics: Ferroelectrics", 162, 665–685, 1994

[1.3] Hill N. A.; "Why are there so few magnetic ferroelectrics?", J. Phys. Chem. B 104, 6694–-6709, 2000.

[1.4] Martin L. W., Crane S. P., Chu Y-H, Holcomb M. B., Gajek M., Huijben M., Yang C. H., Balke N., Ramesh R.; "Multiferroics and magnetoelectrics: thin films and nanostructures", J. Phys., 20:434220–434232, 2008.

[1.5] Wu W., Wu Z., Yu T., Jiang C., Kim W. S.; "Recent progress on magnetic iron oxide nanoparticles: synthesis, surface functional strategies and biomedical applications", April 28, 2015.

[1.6] Martin L. W., Crane S. P., Chu Y. H., Holcomb M. B., Gajek M., Huijben M., Yang C. H., Balke N., Ramesh R.; "Multiferroics and magnetoelectrics: thin films and nanostructures", Journal of physics: Condensed Matter., Published–2008.

[1.7] Zhang S. X., Luo W. J., Wang D. J., Ma Y. W.; Mater. Lett. 63, 1820, 2009.

[1.8] Yu B. F., Li M. Y., Wang J., Pei L., Guo D. Y., Zhao X. Z.; J. Phys. D, Appl. Phys., 41, 185401, 2008.

[1.9] Chu Y-H *et al,* Nat. Mater. 7, 478, 2008.

[1.10] Teague J. R., Gerson R. and James W. J.; Solid State Commun, 8,1073, 1970.

[1.11] Fischer P., Polomska M., Sosnowska I. and Szymanski M; J. Phys. C: Sol. Stat. Vol.13, 1931, 1980.

[1.12] Bader S. D. and Parkin S. S. P.; "Spintronics", Annual Review of Condensed Matter Physics, Vol.1: 71 – 88, August 2010.

[1.13] Adhlakha N., Yadav K. L.; "Study of structural, dielectric and magnetic behavior of $Ni_{0.75}Zn_{0.25}Fe_2O_4$–$Ba(Ti_{0.85}Zr_{0.15})O_3$ composites", Smart Mater Struct., 21:115021–115029, 2012.

[1.14] Kumar M., Yadav K. L.; "Magnetoelectric characterization of $x[Ni_{0.75}Co_{0.25}Fe_2O_4]$ - $(1-x)BiFeO_3$ nanocomposites", J. Phys. Chem. Solids, 68:1791–1795, May 2007.

[1.15] Devan R. S., Kanamadi C. M., Lokare S. A., Chougule B. K.; "Electrical

properties and magnetoelectric effect measurement in x [$Ni_{0.8}Cu_{0.2}Fe_2O_4$] +(1 - x) [$Ba_{0.9}Pb_{0.1}Ti_{0.9}Zr_{0.1}O_3$] composites, Smart Mater Struct., 15:1877–1881, 2006.

[1.16] Dai H., Li T., Xue R., Chen Z.; "Effects of Europium Substitution on the Microstructure and Electric properties of Bismuth Ferrite Ceramics", Journal of Superconductivity and Novel Magnetism, Volume 25, PP.109-115, June 2011.

[1.17] Yang S.Y., Seidel J., Byrnes S. J., Shafer P., Yang C. H., Rossell M. D., Yu P., Chu Y. H., Scott J. F., Ager J. W., Martin L.W., Ramesh R.; "Above-Bandgap Voltages from Ferroelectric Photovoltaic Devices", Nature Nanotechnology, 5: 143–147, Doi:10.1038/nnano.2009.451, 2010.

[1.18] Kadomtseva A. M., Popov Y. F., Pyatakov A. P, Vorob'ev G. P., Zvezdin A. K. and Viehland D.; Phase Transitions, 79, 1019–1042, 2006.

[1.19] Kaur M. and Poonam K. L. Y.; Journal of Materials Science: Materials in Electronics, 27, 4475–4482, 2016.

[1.20] Hossain S. M., Mukherjee A., Chakraborty S., Yusuf S. M., Basu S. and Pal M.; Materials Focus, 2, 92–98, 2013.

[1.21] Mukherjee A., Basu S., Green L. A. W., Thanh N. T. K. and Pal M.; Journal of Materials Science, 50, 1891–1900, 2015.

[1.22] Arya G. S. and Negi N. S., Journal of Physics D: Applied Physics, 46, 95004, 2013.

[1.23] Mukherjee A., Basu S., Chakraborty G. and Pal M., Journal of Applied Physics, 112, 2012.

[1.24] Hossain S. M., Mukherjee A., Basu S. and Pal M., Micro and Nano Letters, 8, 374–377, 2013.

[1.25] Mukherjee A., Banerjee M., Basu S., Mukadam M. D., Yusuf S. M. and Pal M.; Materials Chemistry and Physics, 162, 140–148, 2015.

[1.26] Mukherjee A., Banerjee M., Basu S., Nambissan P. M. G. and Pal M.; Journal of Physics D: Applied Physics, 46, 495309, 2013.

[1.27] Mukherjee A., Basu S., Manna P. K., Yusuf S. M. and Pal M.; Journal of Materials Chemistry C, 2, 5885, 2014.

[1.28] Uniyal P. and Yadav K. L.; Journal of Alloys and Compounds, 511, 149–153, 2012.

[1.29] Editor G., Pearton S., Richeter S., Raehm L., Allen B. L., Keddie M. B. and Star A.; Nanoscale, 2, 1057, 2010.

[1.30] Dutta D. P., Mandal B. P., Naik R., Lawes G. and Tyagi A. K.; Journal of Physical Chemistry C, 117, 2382– 2389, 2013.

[1.31] Dai H., Li T.; Xue R.; Chen Z.; "Effects of Europium Substitution on the Microstructure and electric Properties of Bismuth Ferrite Ceramics." J. Superconductor. Nov. Magn., 25: 109-1154, 2012.

[1.32] Freitas V. F., Grande H. L. C., de Medeiros S. N., Santos I. A., Cótica L. F. and Coelho A. A.; Journal of Alloys and Compounds, 461, 48–52, 2008.

[1.33] Liu J., Fang L., Zheng F., Ju S., Shen M.; "Enhancement of magnetization in Eu doped BiFeO3 nanoparticles", Applied Physics Letters, 95, 022511, 2009.

[1.34] Zhang X., Sui Y., Wang X., Wang Y. and Wang Z.; Journal of Alloys and Compounds, 507, 157–161, 2010.

[1.35] Chen Q., Du P., Huang W., Jin L., Weng W., Han G.; Appl. Phys. Lett., 90, 132907, 2007.

[1.36] Sugimoto M.; Ceram. J. Am. Soc., 82 (2), 269, 1999.

[1.37] Smit J., Wijn H. P. G.; Ferrites, 136, 1959.

[1.38] Ali M. A., Khan M. N. I., F.-U.-Z. Chowdhury, Akhter S., Uddin M. M.; J. Sci. Res., 7, 65, 2015.

[1.39] Topfer J., Murbe J., Angermann A., Kracunovska S.; Int. J. Appl. Ceram. Technol., 3, 455, 2006.

[1.40] Brito VLO, Migliano ACC, Lemos L.V., Melo FCL ; Ceramic processing route and characterization of a Ni–Zn ferrite in application in a pulsed-current monitor. Prog. Electromag. Res., 91:303–318, 2009.

[1.41] Matsushita N., Kond K., Yoshida S., Tada M., Yoshimura M., Abe M.; "Ni-Zn ferrite synthesized from aqueous solution usable for sheet-type conducted noise suppressors in GHz range", J. Electroceram, 16:557-560, 2006.

[1.42] Prasad M. S. R., Prasad B. B. V. S. V., Rajesh B., Rao K. H., Ramesh K. V.; J. Magn. Magn. Mater., 323,2115–2121, 2011.

[1.43] Kaiser M.; Physica B 407, 606, 2012.

[1.44] Jan Čárik V., UŠák E., Šoka M., UŠáková M.; Acta Physica Pol., A 126, 90, 2014.

[1.45] Kwon M. Yoon, Lee M. Y., Mustaqima M., Liu C., Lee B.W.; J. Magn. 19, 64, 2014.

[1.46] Ateia E. E., Ahmed M. A., Salah L. M., El-Gamal A. A.; Physica B, 445, 60,

2014.

[1.47] Wang S. F., Hsu Y. F., Chou K. M., Tsai J.T.; J. Magn. Magn. Mater., 374, 402, 2015.

[1.48] Ashtar M., Maqsood A., Anis-ur-Rehman M.; J. Nanomater. Mol. Nanotechnol., 5, 3, 2016.

[1.49] Ishaque M., Khan M. A., Ali I., Athair M., Khan H. M., Iqbal M. A., Islam M. U., Warsi M. F.; Mater. Sci. Semi. Proc., 41, 508, 2016.

[1.50] Hashim M., Alimuddin, S. Kumar, Ali S., Koo B. H., Chung H., Kumar R.; J. Alloy. Comp., 511, 107, 2012.

[1.51] Köseoğlu Y.; Ceram. Int. 41 (Part A), 6417, 2015.

[1.52] Kumar R., Kumar H., Kumar M., Singh R. R., Barman P. B.; J. Super. Nov Magn., 28, 3557, 2015.

[1.53] Hedayati K.; J. Nanostructure, 5, 13, 2015.

[1.54] Dhanalakshmi B., Pratap K., Rao B. P., Rao P. S. V. S.; "Impedance spectroscopy and dielectric properties of multiferroic $BiFeO_3/Bi_{0.95}Mn_{0.05}FeO_3 - Ni_{0.5}Zn_{0.5}Fe_2O_4$ composites", Ceram. Int: October 2, 2015.

[1.55] Adhlakha N.; Yadav K. L.; "Structural, dielectric, magnetic, and optical properties of $Ni_{0.75}Zn_{0.25}Fe_2O_4–BiFeO_3$ composites", J. Mater. Sci., 49:4423-4438, 2014.

[1.56] Mazumder S. C., Khan M. N. I., Md. Fakhrul Islam, Akhter Hossain A. K. M., "Enhanced multiferroic properties in $(1-y)BiFeO_3–y[Ni_{0.5}Cu_{0.05}Zn_{0.45}Fe_2O_4]$ composites", JMMM 390, 61-69, 2015.

[1.57] Boomgaard JVD, Terrell DR, Born RAJ, Giller HFJI; "An in situ grown eutectic magnetoelectric composite material", J. Mater. Sci.,9:1705–1709, 1974.

[1.58] Boomgaard JVD, Run AMJGV, Suchtelen JV; "Magnetoelectricity in piezoelectric–magnetostrictive composites", Ferroelectrics, 14:727–728, 1976.

[1.59] Chen Z., Li Y., Wu Y.,; "Hydrothermal synthesis and mechanism and property study of La-doped $BiFeO_3$ ceramic", Cer. Intern., 38, 243 – 249, 2012.

[1.60] Yang H., Wang H., He L., Shui L., Yao X., "Polarization relaxation mechanism of $Ba_{0.6}Sr_{0.4}TiO_3/Ni_{0.8}Zn_{0.2}Fe_2O_4$ composite with giant dielectric constant and high permeability", J. Appl. Phys., 108:074105–074110, 2010.

[1.61] Fawzi A. S., Sheikh A. D., Mathe V. L.; "Composition dependent electrical, dielectric, magnetic and magnetoelectric properties of $(x)Co_{0.5}Zn_{0.5}Fe_2O_4$ + (1 -

x)PLZT composites", J. Alloys. Compd., 493:601–608, 2010.

[1.62] Babu S. N, Hsu J. H., Chen Y. S., Lin J. G.; "Dielectric, magnetic and magnetoelectric properties of multiferroic $BiFe_{0.5}Cr_{0.5}O_3$–$NiFe_2O_4$ composites", J. Appl. Phys., 107:09D919–09D921, 2010.

CHAPTER-II

[2.1] Schmid H.; "Some symmetry aspects of ferroics and single phase multiferroics", Journal of Physics: Condensed Matter, 20, art. no. 434201, 2008.

[2.2] Nan C. W.; "Multiferroic magnetoelectric composites: Historical perspective, status, and future directions", J. App. Phys., 103: 031101, 2008.

[2.3] Khomskii D., "Classifying multiferroics: Mechanisms and effects", Physics 2, 20, 2009.

[2.4] Dzyaloshinskii I.; "Magnetoelectricity in ferromagnets", EPL. 83: 67001, 2008.

[2.5] Cohen R. E.; "Origin of ferroelectricity in perovskite oxides", Nature, 358, 136–138, 1992.

[2.6] Hill Nicola A.; "Why Are There so Few Magnetic Ferroelectrics?", J. Phys. Chem. , B. 104 (29): 6694–6709, 2000.

[2.7] Shubnikov A. V.; "Symmetry and Antisymmetry of Finite Figures", USSR Academy of Science, Moscow, 1951.

[2.8] Shuvalov L. V. and Belov N. V.; Kristallographya 7, 192, 1962.

[2.9] Shuvalov L. V. and Belov N. V.; Sov. Phys. Crystallogr., 7, 150, 1962.

[2.10] Khomskii Daniel; "Trend: Classifying multiferroics: Mechanisms and effects", Physics.2., 20, 2009.

[2.11] Melvin M. Vopson; "Fundamentals of Multiferroic Materials and Their Possible Applications", Solid State and Materials Sciences, 0:1–28, 2014.

[2.12] Eerenstein W., Mathur N. D., Scott J. F.; "Multiferroic and magnetoelectric materials", Nature, 759 – 765, 442759 2006.

[2.13] Hu Z., Li M., Yu Y., Liu J, Pei. L., Wang J.; "Effects of Nd and high-valence Mn co-doping on the electrical and magnetic properties of multiferroic $BiFeO_3$ ceramics", Solid State Commun., 150, 1088 – 1091, 2010.

[2.14] Deepti Kothari V., Raghavendra Reddy; "Study of the effect of Mn doping on

the $BiFeO_3$ system", J. Phys. Condens. Matter, 19, 136202, 2007.

[2.15] Kumar M., Yadav K. L.; "Magnetoelectric characterization of $xNi_{0.75}Co_{0.25}Fe_2O_4 – (1-x)BiFeO_3$ nanocomposites", J. Phys. Chem. Solids, 68, 1791–1795, 2007.

[2.16] Kim D. J., Lee M. H., Park J. S.; "Ferroelectric and piezoelectric properties of Mn-modified $BiFeO_3$–$BaTiO_3$ ceramics", J. Electroceram, 37 – 41, 2014.

[2.17] Ryu J., Priya S., Uchino K., Kim H. E.; "Magnetoelectric effect in composites of magnetostrictive and piezoelectric materials", J. Electroceram, 8:107–119, 2002.

[2.18] Bhimasankaram T., Suryanarayana S. V., Prasad G.; "Piezoelectric polymer composite materials", Curr. Sci., 74:967 – 976, 1998.

[2.19] Suchtelen J. V.; "Product properties: a new application of composite materials", Philips Res. Rep., 27:28 – 37, 1972.

[2.20] Lopatin S., Lopatina I., Lisnevskaya I.; Ferroelectrics, 162, 63, 1994.

[2.21] Goldschmidt V. M., "Die Gesetze der Krystallochemie", J. Naturwissenschaften, 14(21), 477 – 485, 1926.

[2.22] Yakel H.; "On the structures of some compounds of the perovskite type", J. Acta Crystallographica, 8(7), 394 – 398, 1955.

[2.23] Tokura Y., Tomioka Y.; "Colossal magnetoresistive manganites", Journal of Magnetism and Magnetic Materials, 200 (1-3), 1–23, 1999.

[2.24] Valenzuela R.; "Magnetic ceramics", Cambridge University Press, Cambridge, 1994.

[2.25] Vestal C. R., Zhang Z. J.; "Magnetic spinel ferrite nanoparticle from microemulsions", Int. J. Nanotech. 1, 240-263, 2004.

[2.26] Harris V. G., Koon N. C., Williams C. M., Zhang Q. and Abe M.; Appl. Phys. Lett., 68, 2082, 1996.

[2.27] Young K. J., Chung W. B., Sangwoo R., Jung-Hoon L., Hyun M. J.; "R3c-R3m Octahedron-tilting transition in rhombohedrally distorted $BiFeO_3$ multiferroics", J. Korean Phys., Soc. 58, 817, 2011.

[2.28] Werner Känzig; "Ferroelectrics and Antiferroelectrics", In Frederick Seitz; T. P. Das; David Turnbull; E. L. Hahn., Solid State Physics.

[2.29] 'Dielectric'. Encyclopedia Britannic.

[2.30] https://www.thebigger.com/physics/electrostatics/what-is-dielectric-polarization

[2.31] https://www.tf.unikiel.de/matwis/amat/elmat_en/kap_3/backbone/r3_3_1

[2.32] https://encyclopedia2.thefreedictionary.com/Dielectric+Loss

[2.33] http://hyperphysics.phy-astr.gsu.edu/hbase/electric/restmp

Chapter III

[3.1] Natalie A. Frey and Shouheng Sun; “Magnetic Nanoparticle for Information Storage Applications”.

[3.2] Torres Y.; Palacio J.; Ortiz J. A.; “Conventional Powder Metallurgy Process and Characterization of Porous Titanium for Biomedical Applications”.

[3.3] www.hielscher.com/sonochem_01.htm

[3.4] Frei, Mark. "Centrifugation Basics". Sigma-Aldrich. Retrieved 10 May 2016.

[3.5] Liao J.Y., Lei B.X., Chen H.Y., Kuang D.B.; “Energy & Environmental” , pubs.rsc.org, 2012.

[3.6] Cullity B. D.; “Elements of x-ray diffraction”

[3.7] Waseda Y.; “X-Ray Diffraction Crystallography Introduction Examples and Solved Problems”.

[3.8] Kasap S.; “Elements of X-ray Diffraction by Crystals”.

[3.9] Kawade V. B., Bichile G. K., Jadhav K. M.; Materials Letters, - Elsevier, 2000

[3.10] Sane A., Sheikh A. D., Mathe V. L.; “Composition dependent electrical, dielectric, magnetic and magnetoelectric properties of (x)$Co_{0.5}Zn_{0.5}Fe_2O_4$ + (1−x)PLZT composites”.

[3.11] http://www.weistron.com/tech-abc/vsm-theory/

[3.12] http://shodhganga.inflibnet.ac.in/bitstream/10603/37018/9/09_chapter%202.pdf

[3.13] Alexander, Chales; Sadiku, Matthew (2006). Fundamentals of Electric Circuits (3, revised ed.). McGraw-Hill.

Chapter IV

[4.1] Fedorchuk A. O. & T. El. Bahraoui *et al.* ; “Multiferroic Eu doped $BiFeO_3$ microparticle polymer composites as materials for laser induced gratings”, J. Mater. Sci: Mater. Electron, 26:9949–9954, 2015

[4.2] Ajmal M., Maqsood A.; “Influence of zinc substitution on structural and electrical properties of $Ni_{1-x}Zn_xFe_2O_4$ ferrites”, Mater. Sci. Eng. B 139:164–170, 2009.

[4.3] Sati P. C. & M. Kumar *et al.*; “Influence of Eu substitution on structural, magnetic, optical and dielectric properties of $BiFeO_3$ multiferroic ceramics” J. ceramint, 10.053. 2014.

[4.4] 52-0278 ICDD, 2002 JCPDS and 89-4926 ICDD, 2002 JCPDS

[4.5] Upadhyay R. V. & H. Parmar *et al.*; "Structural and magnetic properties of nickel–zinc ferrite nanocrystalline magnetic particles prepared by microwave combustion method"; Indian J. Phys., 88(12):1257–1264, December 2014.

[4.6] Ali M. A. & M. M. Uddin *et al.*; "Structural, morphological and electrical properties of Sn-substituted Ni-Zn ferrites synthesized by double sintering technique", Journal of magnetism and magnetic materials 424, 148 – 154, 2017.

[4.7] Adhlakha N. & Yadav K. L.; "Structural, dielectric, magnetic, and optical properties of $Ni_{0.75}Zn_{0.25}Fe_2O_4$ –$BiFeO_3$ composites", J. Mater. Sci., 49:4423 – 4438, 2014.

[4.8] Pattanayak S., Choudhary R. N. P., Das P. R., Shannigrahi S. R.; Ceram. Int. 40, 7983, 2014.

[4.9] Fawzi A. S., Sheikh A. D., Mathe V. L.; Physica B 405, 340, 2010.

[4.10] Yan W., Jiang W., Zhang Q., Li Y. & Wang H.; "Structure and magnetic properties of nickel–zinc ferrite microspheres synthesized by solvothermal method", Materials Science and Engineering B 171, 144 – 148, 2010.

[4.11] Fedorchuk A. O. & T. El. Bahraoui *et al.;* "Multiferroic Eu doped $BiFeO_3$ microparticle polymer composites as materials for laser induced gratings"; J. Mater. Sci: Mater. Electron, 26:9949 – 9954, 2015.

[4.12] Nano Flakes ppromise greater solar energy efficiency' www.gizmag.com. Retrived 2016-02-03.

[4.13] Banerjee M., Mukherjee A., Das D. & Basua S.; "Enhancement of Multiferroic Properties and unusual Magnetic Phase Transition in Eu doped Bismuth Ferrite Nanoparticles", New. J. Chem. August – 2017.

[4.14] Smit J., Wijn H. P. J.; "Ferrites", Philips Technical Library, Eindhoven, Netherlands, 1959 (page 147 - 150).

[4.15] Moon K. W., Cho S. G., Choa Y. H., Kim K. H., Kim J.; "Synthesis and magnetic properties of nano Ba-hexaferrite/Ni-Zn ferrite composites", Phys Status Solidi, A 204:4141 – 4144 , 2007.

[4.16] Babu S. N., Hsu J. H., Chen Y. S., Lin J. G.; "Dielectric, magnetic and magnetoelectric properties of multiferroic $BiFe_{0.5}Cr_{0.5}O_3$ – $NiFe_2O_4$ composites", J. Appl. Phys. 107:09D919–09D921, 2010.

[4.17] Zhang H. F., Or S. W., Chan H. L. W.; "Multiferroic properties of

$Ni_{0.5}Zn_{0.5}Fe_2O_4$ - $Pb(Zr_{0.53}Ti_{0.47})O_3$ ceramic composites", J. Appl. Phys., 104:104109–104114, 2008.

[4.18] http:// en.m.wikipedia/wiki/Exchange_bias.

[4.19] Ali M. A. & Uddin M. M. *et al*.; "Magnetic properties of Sn-substituted Ni-Zn ferrites synthesized from nano-sized Nio, ZnO, Fe_2O_3 and SnO_2", Chinese Physical Society, volume-26 no.7, 2017.

[4.20] Globus A., Duplex P. and Guyot M.; "Determination *of* Initial Magnetization Curve from Crystallites Size and Effective Anisotropy Field" IEEE Trans. Magn., mg-7[3] 617-22, 1971.

[4.21] Snoek J. L.; Physica, 14, 207, 1948.

[4.22] Goldman A.; Modern Ferrite Technology, Springer, Pittsburgh, USA, 2006.

[4.23] ⟨http://encyclopedia2.thefreedictionary.com/Dieelctrics⟩

[4.24] Dai H., Li T., Xue R., Chen Z. & Xue Y.; "Effects of Europium Substitution on the Microstructure and Electric Properties of Bismuth Ferrite Ceramics", J. Supercond. Nov. Magn., 25:109–115, 2012.

[4.25] Devana R. S., Ma Y. R., Chougule B. K.; "Effective dielectric and magnetic properties of (Ni–Co–Cu) ferrite/BTO composites", Mater. Chem. Phys. 115:263–268, 2009.

[4.26] Bhimasankaram T., Suryanarayana S. V., Prasad G.; "Piezoelectric polymer composite materials", Curr. Sci., 74:967–976, 1998.

[4.27] Fechine P. B. A., Almeida A. F. L., Freire F. N. A., Santos M. R. P., Pereira F. M. M., Jimenez R., Mendiola J., Sombra A. S. B.; "Dielectric relaxation of $BaTiO_3$ (BTO)–$CaCu_3Ti_4O_{12}$ (CCTO) composite screen-printed thick films at low temperatures", Mater. Chem. Phys., 96:402–408, 2006.

[4.28] Islam R. A., Priya S.; "Effect of piezoelectric grain size on magnetoelectric coefficient of $Pb(Zr_{0.52}Ti_{0.48})O_3$ – $Ni_{0.8}Zn_{0.2}Fe_2O_4$ particulate composites", J. Mater. Sci., 43:3560–3568, 2008.

[4.29] Belavi P. B., Chavan G. N., Naik L. R.; "Grain size dependent dielectric and magnetic properties of (y)NCCF + (1 -y)BTO particulate composites", Int. J. Nanosci., 11:1240007–1240011, 2012.

[4.30] Islam R. A., Priya S.; "Progress in dual (piezoelectric–magnetostrictive) phase magnetoelectric sintered composites", Adv. Condes. Matter. Phys., 2012.

[4.31] Ravinder D., Reddy A. V. R., Ranga G.; "Abnormal dielectric behavior in

polycrystalline zinc substituted manganese ferrite at high frequencies", Mater. Lett. 52, 259, 2002.

[4.32] Debye P.; "Polar molecules", New York: Chem. Catal. Co., 48(43), 1036-1037, 1929.

[4.33] Hassan R., Hassan J., Hashim M., Paiman S., Azis S.; "Morphology and dielectric properties of single sample $Ni_{0.5}Zn_{0.5}Fe_2O_4$ nanoparticles prepared via mechanical alloying", J. Adv. Ceram. 3, 306 –316, 2014.

[4.34] Parvatheeswara Rao B., Rao K. H.; "Effect of sintering conditions on resistivity and dielectric properties of Ni – Zn ferrites", J. Mater. Sci. 2, 6049 – 6054, 1997.

[4.35] Jadhav R. N., Mathad S. N., Puri V.; "Studies on the properties of $Ni_{0.6}Cu_{0.4}Mn_2O_4$ NTC ceramic due to Fe doping", Ceram. Int., 38 5181 – 5188, 2012.

[4.36] A.A. Hirsch; N. Friedman & S. Bazian, 'The Effect of Frequency on the Electrical Resistivity of Granular metal Films' vacuum, volume-14, Issue-10, October-1964, Pages 393-394

CONFERENCE PUBLICATIONS

1. Al-Masud, S. S. Sikder, M. K. Hasan, Z. Begum and M. N. I. Khan; "Structurel, Electric and Magnetic Properties of (1-x)[$Bi_{0.9}Eu_{0.1}FeO_3$ + x[$Ni_{0.5}Zn_{0.5}Fe_2O_4$] Nanostructured Multiferroic Composites", International Conference on-2018, 08-10 March 2018.
2. Al-Masud, M. N. I. Khan and S. S. Sikder; "Structural, Morphological and Electrical Properties (1-x)[$Bi_{0.9}Eu_{0.1}FeO_3$+x[$Ni_{0.5}Zn_{0.5}Fe_2O_4$] Nano-Structured Multiferroic Composites", Conference onWeather Forecasting & Advances in Physics, 11-12 May 2018.
3. Al-Masud, M. N. I. Khan and S. S. Sikder; "Magnetic Properties of Multiferroic (1-x)[$Bi_{0.9}Eu_{0.1}FeO_3$+x[$Ni_{0.6}Zn_{0.4}Fe_2O_4$] Composites", Conference onWeather Forecasting & Advances in Physics, 11-12 May 2018.